LITHOS 428-429 (2022) 106831

Contents lists available at ScienceDirect

LITHOS

journal homepage: www.elsevier.com/locate/lithos

Research Article

Observational and theoretical evidence for frictional-viscous flow at shallow crustal levels

Carolyn Boulton [a,*], Marcel Mizera [a,b], André R. Niemeijer [b], Timothy A. Little [a], Inigo A. Müller [b], Martin Ziegler [b], Maartje F. Hamers [b]

[a] School of Geography, Environment and Earth Sciences, Victoria University of Wellington, New Zealand
[b] Faculty of Geosciences, Utrecht University, the Netherlands

ARTICLE INFO

Keywords:
Friction
Pressure solution creep
Frictional-viscous flow
Rheology
Clumped isotope thermometry
Mélange

ABSTRACT

Along the Hikurangi Subduction Margin, accretionary prism uplift has exposed the Hungaroa fault zone, an inactive thrust developed within the Middle to Late Eocene Wanstead Formation. Within the ~33 m-wide fault core, deformation of the smectitic, calcareous mudstone matrix produced a penetrative foliation that locally wraps around clasts. Deformation occurred at temperatures constrained by syntectonic calcite vein clumped isotope thermometry, which yielded a narrow range of Δ_{47} values between 0.445 ± 0.024‰ and 0.482 ± 0.013‰, corresponding to a mean calcite precipitation temperature of 82^{+13}_{-12} °C. Optical and scanning electron microscopy analyses reveal that calcite underwent: dissolution along stylolites and clast, vein, and microlithon margins; precipitation in foliation-parallel and foliation-perpendicular extension veins; and precipitation in hybrid veins and strain fringes. Maximum differential stress estimates obtained from calcite twin densities (44.1 ± 13.9 to 96.6 ± 20.8 MPa) are consistent with those sustainable by a cohesionless fault at ~3 km depth with a friction coefficient in the range measured for two calcareous mudstones ($\mu = 0.38$ to 0.50) and a micrite clast ($\mu = 0.61$ and 0.64). Marlstone clasts within the foliated calcareous mudstone matrix contain mutually cross-cutting shear fractures and extension veins with crack-seal textures, providing evidence for temporal fluctuations in shear strength resulting from pore fluid overpressure transients. At strain rates imposed during laboratory experiments, frictional sliding involves granular flow processes. Yet, calcite microstructures indicate that diffusive mass transfer played an important role in accommodating deformation. We model the fault zone rheology assuming diffusion-controlled frictional-viscous flow, with deformation at strain rates $\dot{\gamma} \leq 10^{-9}$ s^{-1} able to have taken place at very low shear stresses ($\tau < 10$ MPa) given sufficiently short diffusion distances ($d < 0.1$ mm), even in the absence of pore fluid overpressures. However, if grain-scale and fracture-scale processes change the diffusion distance, fault zones deforming via frictional-viscous flow can exhibit temporally variable strain rates. Thus, our results suggest that the shallow (up-dip) limit of the seismogenic zone is not a simple function of temperature in fault zones governed by a frictional-viscous flow rheology.

1. Introduction

Accumulated elastic strain drives earthquake rupture nucleation and propagation. Between earthquakes, creeping patches and locked asperities on crustal faults control the distribution of accumulated elastic strain and thus seismic potential (e.g., van den Ende et al., 2020; Wang et al., 2021). Yet the frictional and frictional-viscous processes that facilitate creep on shallow crustal faults, such as shallow subduction zone décollements, remain poorly understood (e.g., Fagereng and Beall, 2021; Gratier et al., 2013; Tesei et al., 2013). At mid-to-low latitudes, calcareous sediments are important subduction zone input materials, and calcite-bearing lithologies form faults in diverse structural settings worldwide (e.g., Ebert et al., 2007; Kurzawski et al., 2018; Leah et al., 2020; Molli et al., 2011; Plank, 2014; Smeraglia et al., 2018). Compared with siliclastic lithologies, calcareous rocks more readily accommodate strain aseismically via crystal plasticity and diffusive mass transfer processes at low temperatures and pressures in the upper crust (e.g., Bauer et al., 2018; Kennedy and White, 2001; Renard et al., 2000;

* Corresponding author.
E-mail address: carolyn.boulton@vuw.ac.nz (C. Boulton).

https://doi.org/10.1016/j.lithos.2022.106831
Received 20 February 2022; Received in revised form 26 July 2022; Accepted 2 August 2022
Available online 6 August 2022

Rutter, 1976). Since aseismic creep can limit seismic potential, quantifying the rheology of calcareous rocks is societally relevant and scientifically important.

Traditionally, researchers have taken two main approaches to understanding the deformational behaviour (rheology) of fault rocks. In the first approach, faults that have undergone slip at spatiotemporally variable, slow-to-fast, strain rates are mapped and described at multiple scales that capture the kinematics and dynamics of faulting as well as the grain-scale deformation mechanisms that accommodated strain (e.g., Mizera et al., 2020, 2021; Sibson, 1977; Tesei et al., 2013). A complementary approach involves simulating fault slip in rock deformation experiments, in which mineralogy, temperature, applied stress, strain rate, and pore fluid pressure can be carefully controlled (e.g., Bos et al., 2000a, 2000b; Collettini et al., 2019; De Bresser, 2002; Faulkner et al., 2018; Niemeijer and Spiers, 2005; Rutter, 1976). That experiments must be performed at strain rates orders of magnitude higher than plate rates is a well-documented limitation of laboratory rock deformation (e.g., Passchier and Trouw, 2005); to overcome this, researchers have developed experimentally validated microphysical models of slip that can be extrapolated to geological strain rates if the same

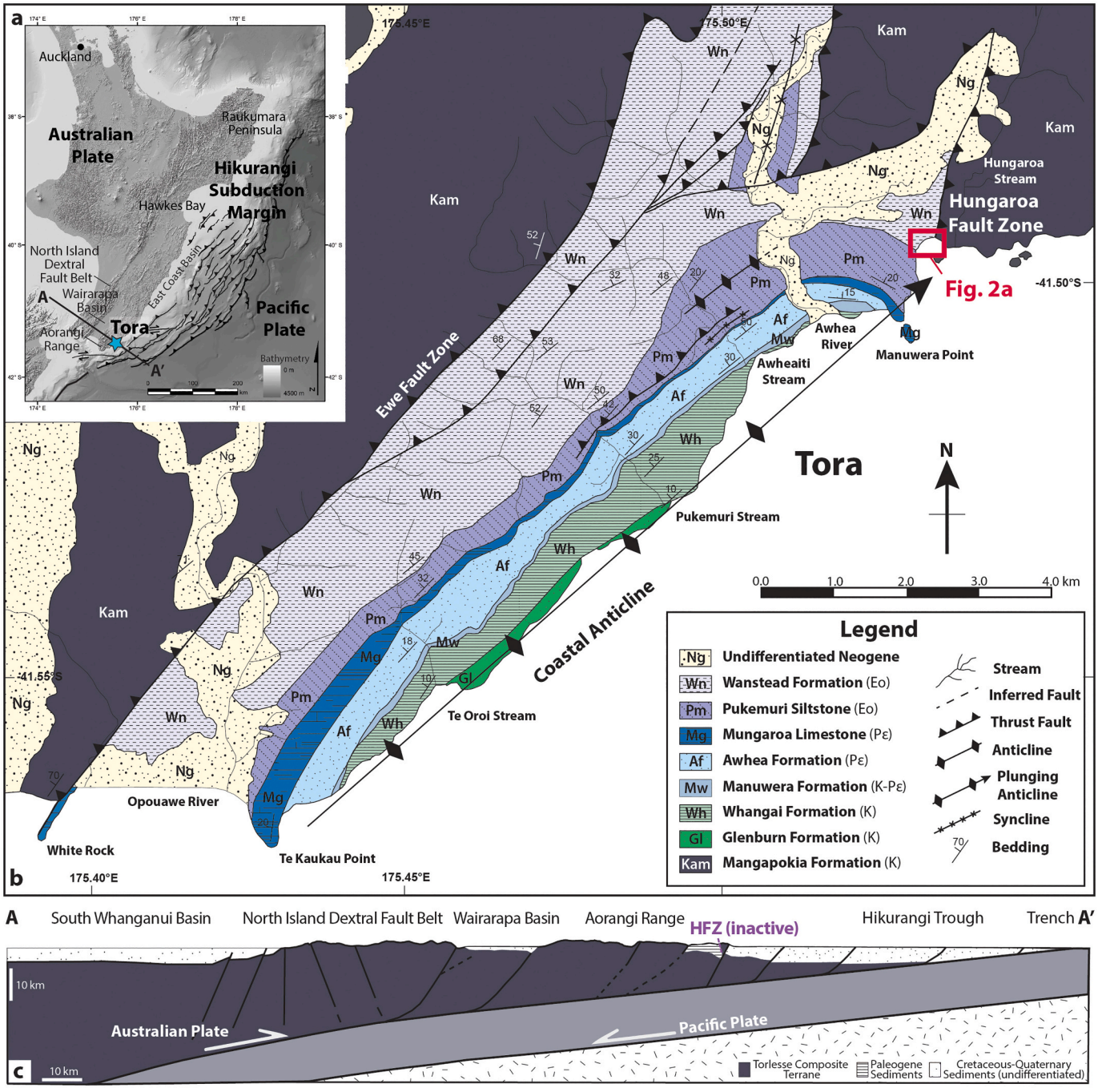

Fig. 1. Tectonic setting of the Hikurangi Subduction Margin and the Hungaroa fault zone at Tora, SE Wairarapa coast. (a) Bathymetry and topographic map of the North Island, New Zealand. Active faulting of the onshore and offshore subduction margin is indicated by black lines (after Ghisetti et al., 2016). Blue star indicates location of the Tora study locality and A-A' delimits the cross-section location in (c). (b) Geological map of the Upper Cretaceous–Lower Paleogene sequence at Tora (after Hines et al., 2013). (c) Schematic cross-section of the southern HSM depicting the Hungaroa fault zone (HFZ) (after Hines et al., 2013 and Henrys et al., 2013). (For interpretation of the references to colour in this figure legend, the reader is referred to the web version of this article.)

deformation mechanisms are operating (e.g., Bos and Spiers, 2002). A particularly powerful method used to constrain fault rheology involves combining geological observations of natural fault zones with microphysics-based constitutive equations derived from laboratory experiments (e.g., French and Condit, 2019; Phillips and White, 2017; Wallis et al., 2015).

Along the Hikurangi Subduction Margin (HSM) of New Zealand, accretionary prism uplift has exposed the Hungaroa fault zone (HFZ), a previously undocumented, inactive thrust fault developed within fine-grained, calcareous sedimentary rocks (Fig. 1) (Hines et al., 2013). Nearly continuous exposure along a coastal section enabled detailed mapping of the footwall, fault core, and hanging wall of this fault, and it provided an unparalleled opportunity to document deformation in sediments lithologically akin to those that currently form the shallow Hikurangi Subduction Zone décollement (Barnes et al., 2020; Ghisetti et al., 2016). Using multidisciplinary structural geology, quantitative X-ray diffraction, microstructural analysis, isotope geochemistry, and experimental rock deformation methods, we describe tectonites developed at shallow depths (<4 km) within the fault core, quantify the temperature and stress conditions under which they experienced deformation, identify the operative deformation mechanisms, and place experimental and theoretical constraints on the strength of the fault zone at strain rates spanning the full range of subseismic fault slip.

2. Geological background

2.1. Tectonic setting

Propagation of the Pacific-Antarctic spreading ridge system rent Zealandia away from Gondwana in the Late Cretaceous (90–83 Ma) (e.g., Mortimer et al., 2019). Following rifting, Zealandia underwent widespread cooling and subsidence until the Late Oligocene to Early Miocene (30–20 Ma), when southwards migration of the Tonga-Kermadec trench formed the Hikurangi Subduction Margin, along which the Pacific Plate subducts beneath the Australian Plate (Ballance, 1976; Nicol et al., 2007) (Fig. 1a). Early stages of subduction (~25–18 Ma) were associated with allochthon emplacement (Sutherland et al., 2009) and large-displacement thrust faulting as the passive margin collapsed and contracted (Chanier and Ferriere, 1991; Delteil et al., 1996; Nicol et al., 2007; Pettinga, 1982; Rait et al., 1991). From its inception until the Late Miocene (~10 Ma), the HSM was oriented nearly orthogonal to the plate motion vector, resulting in margin-wide compression, excepting some extension in the Hawkes Bay region (Barnes et al., 2002). Over the past ~25 Ma, migration of the Australian/Pacific relative Euler vector and clockwise rotation of the HSM of 45° to 80° has resulted in increasing amounts of plate motion obliquity and strike-slip faulting (e.g., Furlong and Kamp, 2009; Lamb, 2011; Nicol et al., 2007). The current phase of HSM deformation, characterized by upper plate transpression south of Hawkes Bay, began by the Early Pleistocene (2–1 Ma) (e.g., Nicol and Wallace, 2007). Strike-slip faults in the North Island Dextral Fault Belt, aided by some fore-arc rotation, had evolved by this time to accommodate most of the margin-parallel motion (Beanland and Haines, 1998; Jiao et al., 2015). East of the North Island Dextral Fault Belt, sediments of the Wairarapa Basin and basement rocks of the Aorangi Range act as a deformable backstop to an offshore accretionary wedge developed mainly since the Late Pliocene (Barnes et al., 1998; Ghisetti et al., 2016) (Fig. 1). In the study area, 42 $mmyr^{-1}$ of present-day relative plate motion resolves into ~28 $mmyr^{-1}$ parallel to the margin and ~30 $mmyr^{-1}$ perpendicular to the margin (Beavan et al., 2002). Over 85% of the margin-perpendicular deformation is accommodated by the subduction zone megathrust fault (Nicol et al., 2007).

2.2. Stratigraphy

The Tora study area lies within the East Coast Basin (ECB), a slope and fore-arc basin complex that stretches along the eastern HSM (Fig. 1). The ECB basement consists of a Permian to Early Cretaceous flysch sequence (Torlesse Composite Terrane, including the Mangapokia Formation at Tora) accreted onto the margin of Gondwana prior to rifting in the Late Cretaceous (Begg and Johnston, 2000; Mortimer, 2004). As the Tasman Sea opened, sedimentation rates declined, resulting in a Late Cretaceous unconformity upon which siliclastic sedimentary rocks of the Glenburn and Whangai Formations (Late Cretaceous to Paleocene) were deposited on the more deformed, accreted sedimentary rocks of the Torlesse Composite Terrane. Continued subsidence resulted in a fining upwards succession. Sandstones in the Awhea Formation (Early Paleocene) transition upwards into the Mungaroa Limestone (Early to Late Paleocene), the top of which forms an erosional contact with calcareous sandstones and siltstones of the overlying Awheaiti Formation (Late Paleocene). The Pukemuri Siltstone (Early Eocene) unconformably overlies the Awheaiti Formation and is itself unconformably overlain by calcareous mudstones of the Wanstead Formation (Middle to Late Eocene). This condensed stratigraphic sequence is <600 m-thick and contains no sedimentary rocks younger than Late Eocene (Hines et al., 2013). At Tora, the Paleogene sedimentary rocks were deposited in a transitional setting between dominantly more siliciclastic facies to the north, and dominantly more calcareous facies to the south (Field and Uruski, 1997; Laird et al., 2003).

3. Field observations

3.1. Structural overview and fold analysis

The Hungaroa fault zone is exposed along an approximately 400 m-wide beach at Stony Bay, Tora (Fig. 1). The wave-cut platform and cliffs comprise three main sections (Fig. 2a): (1) the southwestern section, where the Pōhatu fault (new) juxtaposes the Pukemuri siltstone against the Wanstead Formation; (2) the middle section, where Wanstead Formation sedimentary rocks are steeply-dipping, folded, and mainly overturned; and (3) the eastern section, consisting of a high strain zone ~33 m-thick (33.6 m-wide along the cliff-parallel measured section in Fig. 2), hereafter termed the Hungaroa fault core. This tabular zone is bounded by the Hungaroa fault to the east, which separates Mangapokia Formation sedimentary rocks from those of the Wanstead Formation (Fig. 2a). Structural measurements in the following subsections are reported with reference to the eastern bounding Hungaroa fault, which dips steeply with a mean strike/dip direction/dip of 012/SE/77 (Fig. 2b–e).

At the western end of Stony Bay, calcareous mudstones of the Wanstead Formation are juxtaposed, to the west, against the Pukemuri Siltstone by the Pōhatu fault (037/SE/80), a 30 cm-wide zone of cataclasite containing mm to cm-sized, sub-angular clasts of siltstone in a matrix of calcareous clays (Fig. 2a). At Pukemuri Stream (Fig. 1), the boundary between the two formations was formally described as an unconformity that includes a 1 m-thick basal conglomerate (Hines et al., 2013). However, at Stony Bay, the basal conglomerate is absent and the boundary is the Pōhatu fault, which has a down-to-the-east apparent sense of throw. In the western and central sections of Stony Bay, the Wanstead Formation consists mainly of green-grey to blue-grey calcareous smectitic mudstones with minor interbedded glauconitic sandstones and siltstones. Based on younging directions visible in graded sandstone beds, they are predominantly overturned.

The sequence is pervasively deformed, and many beds (here defined as S_0) are folded at half-wavelengths of 10's to 100 cm. The mesoscopic folds have inter-limb angles that range from 55–96° (mostly open) in the west to 9–34° (tightly appressed) further to the east, a transition that reflects an increase in strain magnitude towards the Hungaroa fault (Fig. 2b). In the immediate footwall of the Hungaroa fault, within the fault core, fold inter-limb angles decrease to <8–34° (tight-to-isoclinal folds). Axial surfaces in the fault core are oriented sub-parallel to the Hungaroa fault and dip steeply to the ESE (Fig. 2b). The hingelines of

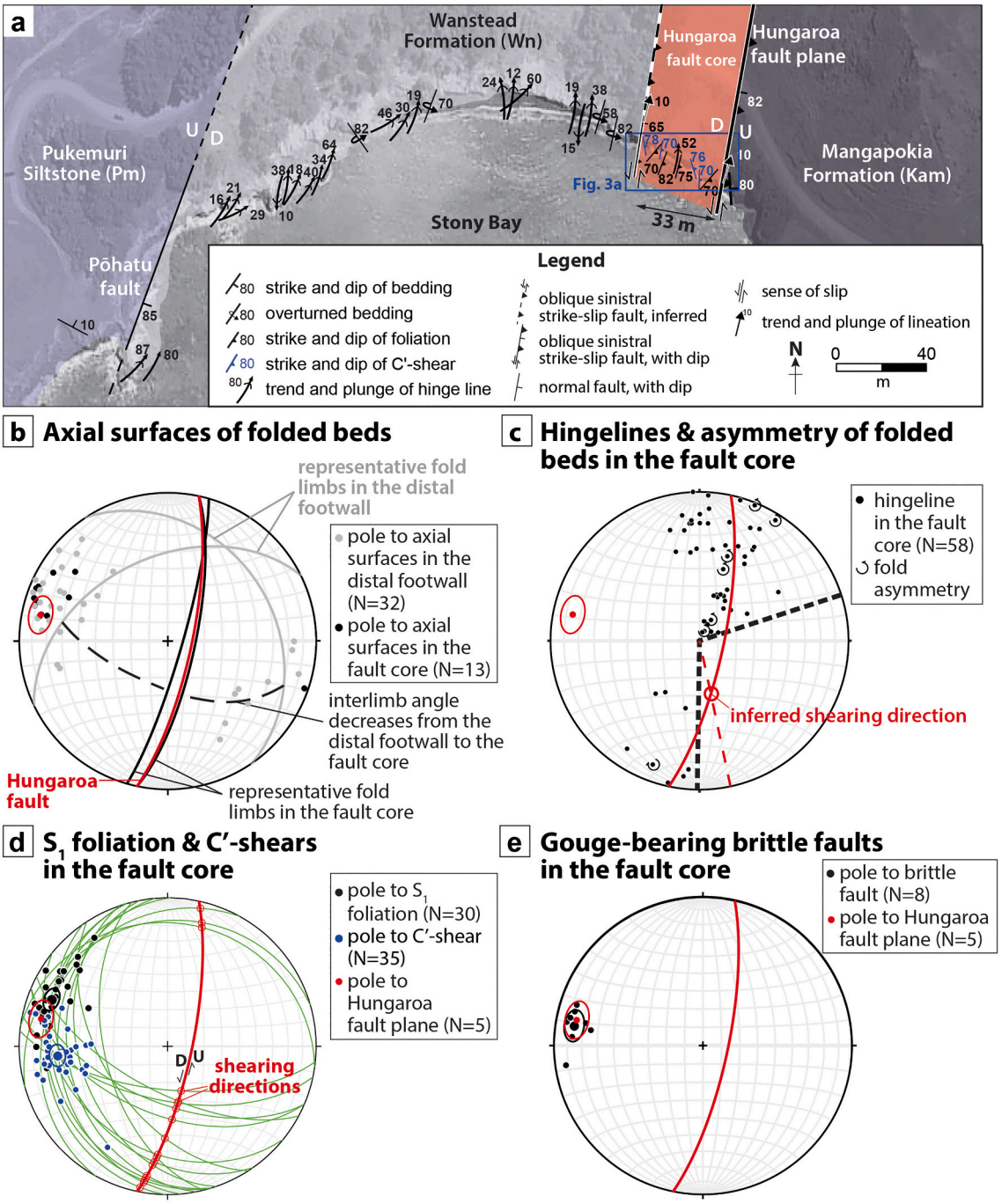

Fig. 2. Structural analysis of the Hungaroa fault zone. (a) Structural map of the Hungaroa fault zone, Stony Bay, Tora. The fault core is highlighted in red; the blue box shows the location of Fig. 3a. (b) Folded Wanstead Formation bedding orientations along the entire section. (c) Orientations of hingelines within the fault core. Arcuate arrows denote observed down-plunge fold asymmetries. The arc of the fault's mean orientation across which the fold asymmetries reverse in sense contains the approximate shearing direction (open red circle) along the bisector of the angle defining this arc (after the method by Hansen, 1971). (d) Poles to the S_1 foliation (black dots) and C′ planes (blue dots). Ellipses around enlarged dots denote mean pole and 95% confident limit. Assuming the shearing plane lies parallel to the Hungaroa fault, inferred shearing directions (open red circles) are given by the intersection of the movement planes (green great circles containing paired S_1 and C′-shear poles) with the fault plane. (e) Poles to gouge-bearing brittle faults (black dots) cross-cutting the S_1 foliation and C′-shears. Figures (b-e) are lower hemisphere equal area stereograms. (For interpretation of the references to colour in this figure legend, the reader is referred to the web version of this article.)

these noncylindrical folds are strongly curved, the folds are sheath-like in outcrop, and the hingeline attitudes are widely dispersed in the mean plane of the Hungaroa fault (Fig. 2c).

3.2. Fault core fabric

A fault ~33 m west of the Hungaroa fault forms the boundary between folded rocks of the Wanstead Formation to the west, which we refer to as the distal footwall, and strongly deformed rocks of the Hungaroa fault core (Fig. 2). This boundary fault contains a ~5 cm-wide dark-grey gouge that is discordant to folded bedding (S_0) in the distal footwall; the fault strikes sub-parallel to the Hungaroa fault and is similarly decorated with calcite slickenfibers that plunge shallowly to the NNE, but it dips less steeply (009/ESE/60) (Figs. 2a, e, 3). East of this

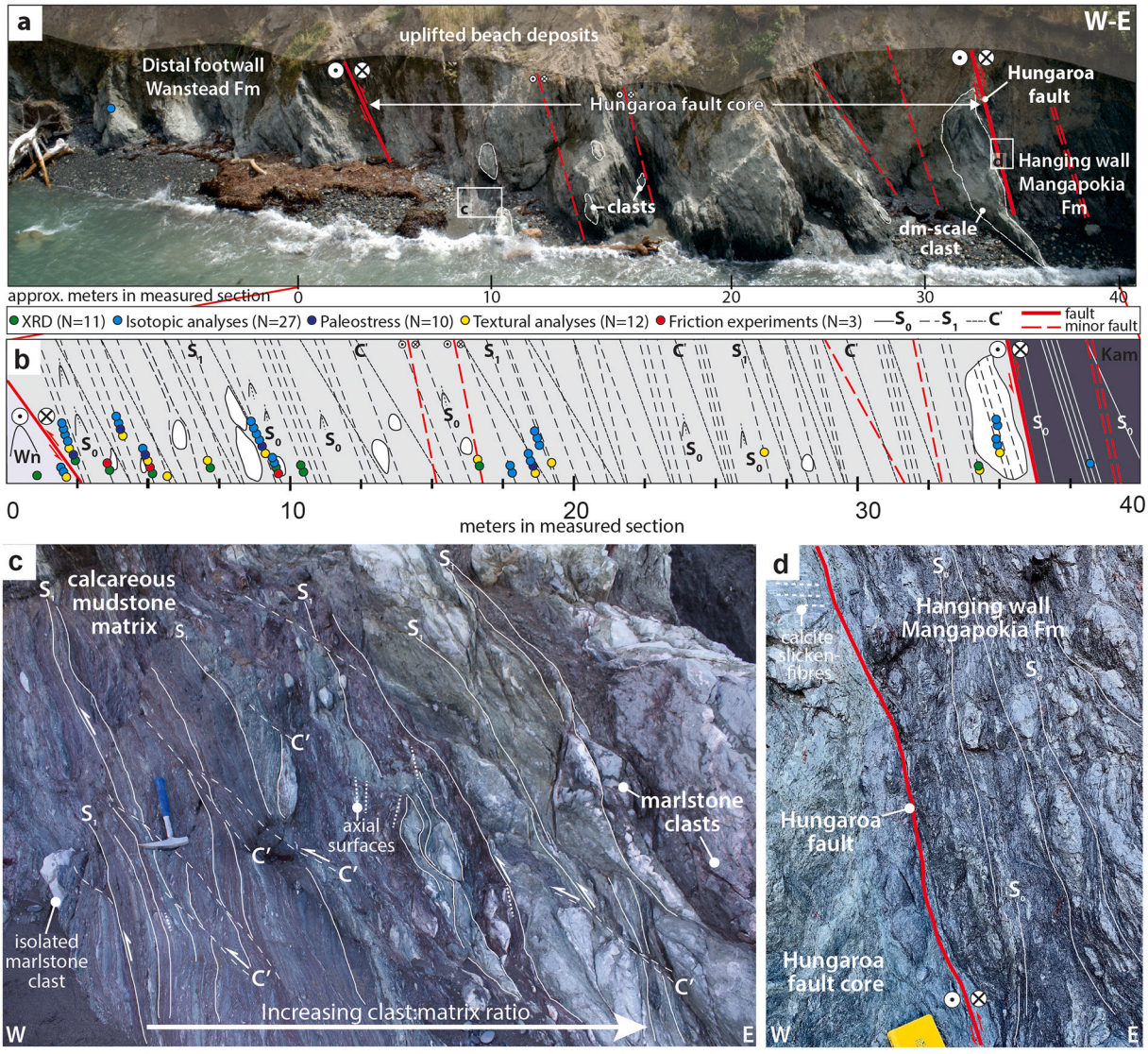

Fig. 3. Hungaroa fault zone. (a) UAV-based outcrop photograph of the Hungaroa fault zone. Scale is approximate, with the locations of (c) and (d) shown by white boxes. (b) Schematic drawing of structural elements within the sheared fault core, showing measured apparent dips. Locations of samples collected and analyses performed (details in legend) given by the intersection of the foliation containing the symbols with the x-axis. (c) Photograph of SC'-tectonites in the Hungaroa fault core. (d) Photograph of the easternmost fault core and Hungaroa fault.

bounding fault, within the fault core, S_0 is strongly dismembered. Calcareous mudstones are overprinted by a pervasive scaly foliation (here defined as S_1) that anastomoses around lenticular fragments of sandstones and marlstones (Fig. 3). On average, S_1 is steeply SE-dipping (022/SE/74) and inclined at a low (~10°) angle to the Hungaroa fault plane (Fig. 2d). Elongate blocks (proportionally: marlstone >> sandstone > siltstone > limestone) occur as cm- to dm-long sigmoidal clasts (phacoids) scattered within, and wrapped by, a sheared calcareous mudstone matrix (Fig. 3c).

This block-in-matrix mélange fabric (Fig. 3a, b) hosts shear bands up to 5 mm-wide marked by a local rotation of S_1 into alignment with the shear bands, analogous to C′-shears in mylonites (Fig. 3c) (e.g., Finch et al., 2020). The shear bands, hereafter termed C′-shears, have a mean orientation of 356/NE/64. The C′ shears are typically inclined at a ~20° anticlockwise angle to the plane of the Hungaroa fault (Fig. 2d). C′-shears are present throughout the fault core, being more closely spaced (at <15–30 cm intervals) in sheared calcareous mudstone and more widely spaced (at meter-intervals or more) in more indurated lithologies such as marlstone (Fig. 3b, c). Both the S_1 foliation and the C′-shears are cross-cut by minor gouge-filled faults that are oriented sub-parallel to the Hungaroa fault (Figs. 2e, 3a, b). These cross-cutting faults host mm- to cm-thick, fine- to ultrafine-grained, red or grey gouges layers that can exhibit foliated and/or random fabrics, described in more detail in Section 4.

Multiple sites of calcite-filled mineralization are distinguishable within the fault core. The main calcite-filled mineralization sites (here referred to as calcite veins) are: (1) parallel to the S_1-foliation, with sites including mm-thick, discontinuous calcite veins hosted in the sheared calcareous mudstones as well as calcite veins that form the tails of rotated and stretched clasts; (2) up to cm-thick calcite veins hosted in limestones, siltstones and marls oriented oblique-to-perpendicular to the S_1-foliation; (3) C′-shear-parallel, mm-thick calcite veins structurally above and/or within the C′ planes; (4) calcite veins in the hinges of the folded and dismembered beds (S_0) of the Wanstead Formation (saddle reef veins); and (5) mm- to cm-thick calcite-dominated slickenfiber veins with slightly curved slickenlines that coat clasts of indurated lithologies. In addition, calcite slickenfibers are present along some brittle faults.

Kinematic indicators (sigmoidal clasts, C′-shears) consistently indicate oblique-sinistral slip relative to the fault's present-day attitude (Fig. 3). The shearing direction in the Hungaroa fault zone can be

estimated from fold hingeline orientations (using the separation arc technique of Hansen, 1971, Fig. 2c) and from the angular disposition of paired S_1 and C′ planes together with the sense of foliation deflection adjacent to those C′-shears (Fig. 2d). In present-day coordinates, all these data indicate a sense of shear that was sinistral and east-side-up (reverse) and a shearing direction that plunged predominantly SSE (Figs. 2, 3).

4. Mineralogical and microstructural observations

4.1. Analytical methods

Detailed microstructural and mineralogical analyses were performed on 38 rock samples collected from outcrops along Stony Bay, with 30 of the samples distributed across the Hungaroa fault core (Fig. 3b). Quantitative X-ray powder diffraction (QXRPD) yielded the mineralogy of 11 fault rock samples comprising calcareous mudstones, marlstones, and a fossiliferous biomicrite (hereafter "micrite") (Folk, 1959; Picard, 1971). From the samples, 22 were oriented perpendicular to foliation and parallel to slickenlines (defined by a fibrous calcite lineation and/or groove lineation) and prepared into thin sections. All samples were labelled according to a measured section location, in metres; the measured section began in the distal footwall 2.7 m west of the fault core bounding fault (Fig. 3b). To investigate deformation mechanisms during fault slip, fault rock microstructures were studied using optical microscopes and a scanning electron microscope (SEM) equipped with electron-backscatter diffraction (EBSD) and energy dispersive spectroscopy (EDS) detectors (Supporting Information S1.2 to S1.5).

4.2. Quantitative X-ray powder diffraction results

Bulk rock QXRPD results reveal that the sheared sedimentary rocks contain 27–60% phyllosilicates (smectite (montmorillonite) > white mica (muscovite/illite) > kaolin), 7–56% calcite, 15–30% quartz, ≤4% feldspar, <1% pyrite and other accessory minerals (Table 1). Marlstones and micrites that form clasts within the scaly fabric contain the least phyllosilicates (up to 27%) and the most calcite (up to 78%). A footwall calcareous mudstone, two fault core calcareous mudstones, and a fault core gouge were selected for further quantitative analysis of the clay fraction with a grain size <2 μm (Supporting information S1.6). Results indicate that the sedimentary rocks comprise, by weight, between 29.8 and 39.7% clay-sized particles. The term calcareous mudstone is used throughout the paper to describe the fine-grained fault core and footwall rocks, but the sedimentary rocks are strictly defined as clayey siltstones given the proportion of clay-sized particles measured (Picard, 1971). Following Ca-saturation and acetic acid treatment to remove carbonates, the QXRPD analyses show that 71 to 86% of the clay fraction is composed of phyllosilicates (smectite (montmorillonite) > white mica (illite/muscovite) > kaolin) (Table 1). The width and location of the clay separates' smectite (001) and (002) peaks indicates little, if any, smectite/illite interstratification in fault core samples HFZ2.7 m and HFZ10.6 m_G. However, there is some smectite/illite interstratification in the distal footwall (FWWanstead) and fault gouge (HFZ16.8 m) samples (Supporting Information S1.6) (Raven et al., 2018).

4.3. Microstructural descriptions of fault core fabric

Within Hungaroa fault core calcareous mudstones, the S_1 foliation is defined by a shape preferred orientation of phyllosilicates (Figs. 3, 4a–g and 5a–c). The S_1 foliation is the primary fabric element present throughout the entire fault core, but it is cross-cut by C′-shears (Figs. 3, 4a–b and g). Within the cross-cutting C′-shears, phyllosilicates and calcite vein fragments are aligned parallel to C′-shear margins, which are commonly coated with calcite veins (Fig. 4g). At four locations, mm-wide gouge-filled faults oriented subparallel to the Hungaroa fault cross-cut both the S_1 foliation and C′-shears (Figs. 3b and 4h–j). Microstructural analyses performed on a gouge-filled fault (sample HFZ16.8 m) reveal that the principal slip surface is a <1 mm-thick ultrafine-grained, phyllosilicate-rich, random-fabric gouge that includes entrained wall-rock fragments (Table 1) (Figs. 3b and 4h–j). A ~2 mm-thick foliated gouge occurs between the random-fabric gouge and wall-rock calcareous mudstones. Within the smectite-rich matrix of the foliated gouge, the foliation is subparallel to the principal slip surface (Fig. 4e and h–j).

To quantitatively characterize the fault core microstructure, the foliation spacing (defined as the short axis of the microlithons) and the aspect ratio of microlithons (defined as the long axis of the microlithons divided by short axis) were measured (Fig. 5). Digital image analysis was conducted on multiple thin section- and SEM-scale images acquired from samples containing representative variations in foliation spacing. Notably, the foliation spacing can vary on the thin section scale when foliation-perpendicular variations in lithology and clast size occur. Within the clay-rich foliated gouges of cross-cutting brittle faults (Fig. 2b), the foliation spacing varies between 0.4 μm and 21 μm, with an average spacing of 3.2 ± 0.6 μm (95% confidence level (CL)) (Fig. 5a, d). In C′ shears, the foliation spacing ranges from 6.0 μm to 120.5 μm, with an average spacing of 42.4 ± 8.8 μm (95% CL) (Fig. 5b, d).

Spacing of the S_1 foliation in sheared calcareous mudstones (external to the C′ shears) ranges between 1.7 μm and ~639.2 μm, with an average spacing of 98.8 ± 14.4 μm (95% CL) (Fig. 5c, d). The broad range of S_1 foliation spacing observed might be explained by variations in the

Table 1
Quantitative XRPD analysis (in wt%) of representative footwall and fault core rocks. Clay fraction analyses performed on separates with a grain size <2 μm.

Sample	Description	Quartz	Calcite	Smectite	White Mica	Kaolin	Plagioclase	Total Phyllosilicates
FWWanstead	Grey Mudstone	22	16	25	17	16	4	58
FWWanstead†	Clay fraction	14	NA	49	18	19		86
HFZ1.1 m	Grey Mudstone	25	35	17	11	10	3	38
HFZ2.7 m^	Dark Grey Mudstone	30	22	24	11	9	3	44
HFZ2.7 m†	Clay fraction	28	NA	42	17	12		71
HFZ3.7 m	Green-grey Marlstone	15	56	20	6	1	2	27
HFZ5.2 m^	Dark Grey Mudstone	27	32	18	11	8	3	37
HFZ7.4 m*	Red Mudstone	19	40	19	12	8	2	39
HFZ9.6 m	Cream Micrite	14	78	7	1		<1	8
HFZ10.6 m_G	Green Mudstone	17	35	33	10	2	3	45
HFZ10.6 m_G†	Clay fraction	17	NA	69	12	2		83
HFZ10.6 m_R	Red Mudstone	17	45	25	10	2	2	37
HFZ16.8 m^	Red Gouge	29	7	28	15	17	4	60
HFZ16.8 m†	Clay fraction	15	NA	52	14	18		84
HFZ34.5 m^	Dark Grey Mudstone	27	17	35	14	3	3	52

* Contains trace amounts of hematite.
^ Contains trace amounts of pyrite.
† Contains trace amounts of anatase.

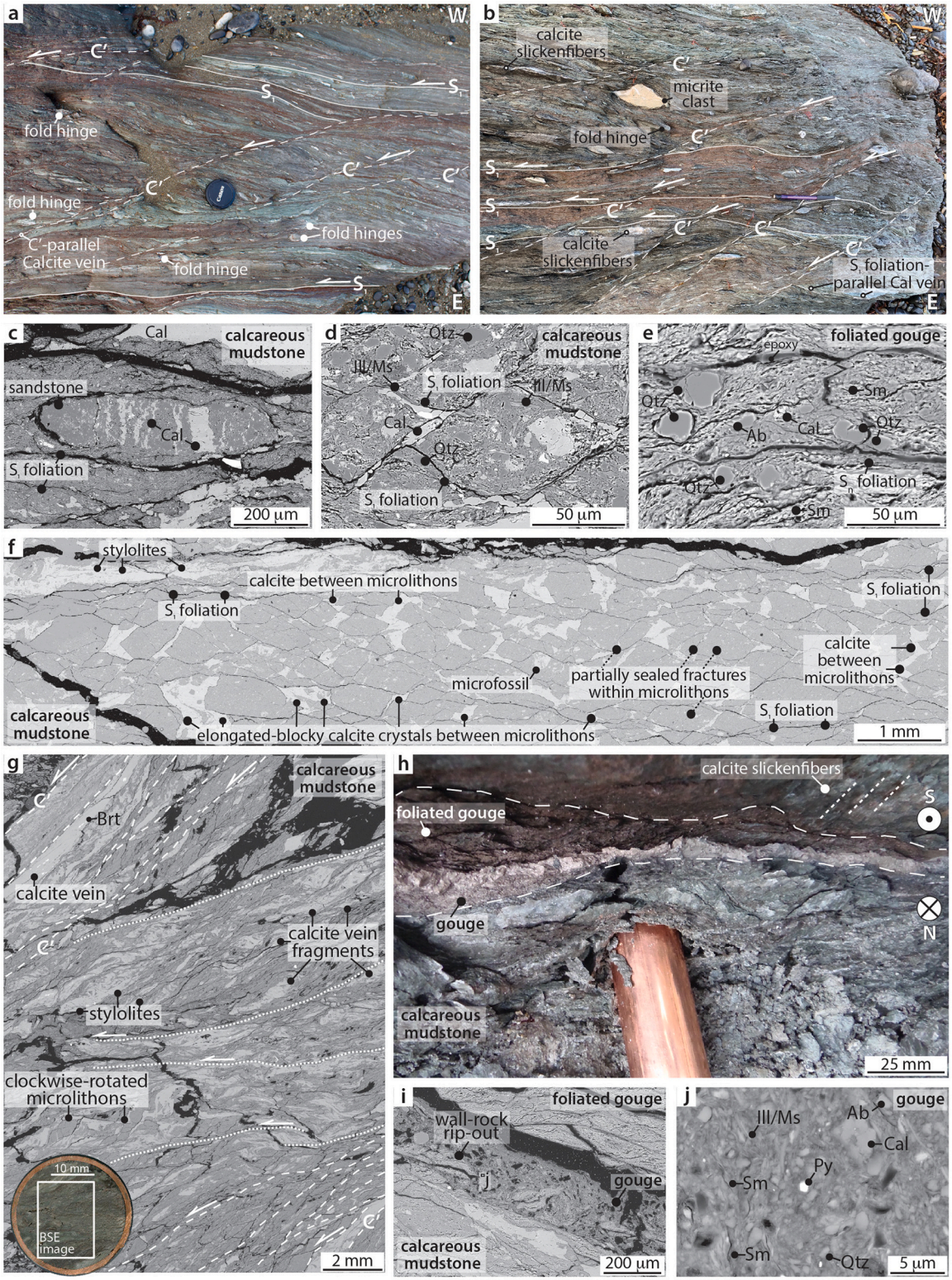

Fig. 4. Fault core fabric elements. (a and b) S_1 foliation and C′-shears in calcareous mudstone located at approximately 7.5 m and 28.5 m, respectively, on the measured section in Fig. 3b. (c) Backscattered electron (BSE) image of a stretched sandstone clast enclosed by S_1 foliation planes (HFZ7.4 m) and containing calcite veins at a high angle to the foliation. (d) BSE image of the S_1 foliation anastomosing around microlithons. Note calcite precipitated between microlithons (HFZ7.4 m). (e) BSE image of a foliated smectite-rich fault gouge (HFZ16.8 m). The small crystallite size and crinkly margins of the matrix clay is diagnostic of smectite (montmorillonite). (f) Stitched BSE images showing the anastomosing S_1 foliation developed in a calcareous mudstone. Note the truncated microfossil, calcite between microlithons, and partially sealed fractures within microlithons (HFZ2.7 m). (g) Stitched BSE images showing a C′-shear cutting across and deflecting the S_1-foliation (HFZ5.75 m). Collected sample within copper pipe, inset. (h) Fault core gouge-filled fault. BSE images of the gouge and foliated gouge are depicted in figures (i) and (j) (HFZ16.8 m). Shear sense is top-to-the-left in all figures apart from (h), where movement is in and out of the page. Mineral abbreviations are: calcite (Cal), quartz (Qtz), albite (Ab), illite/muscovite (Ill/Ms), smectite (Sm), barite (Brt), and pyrite (Py).

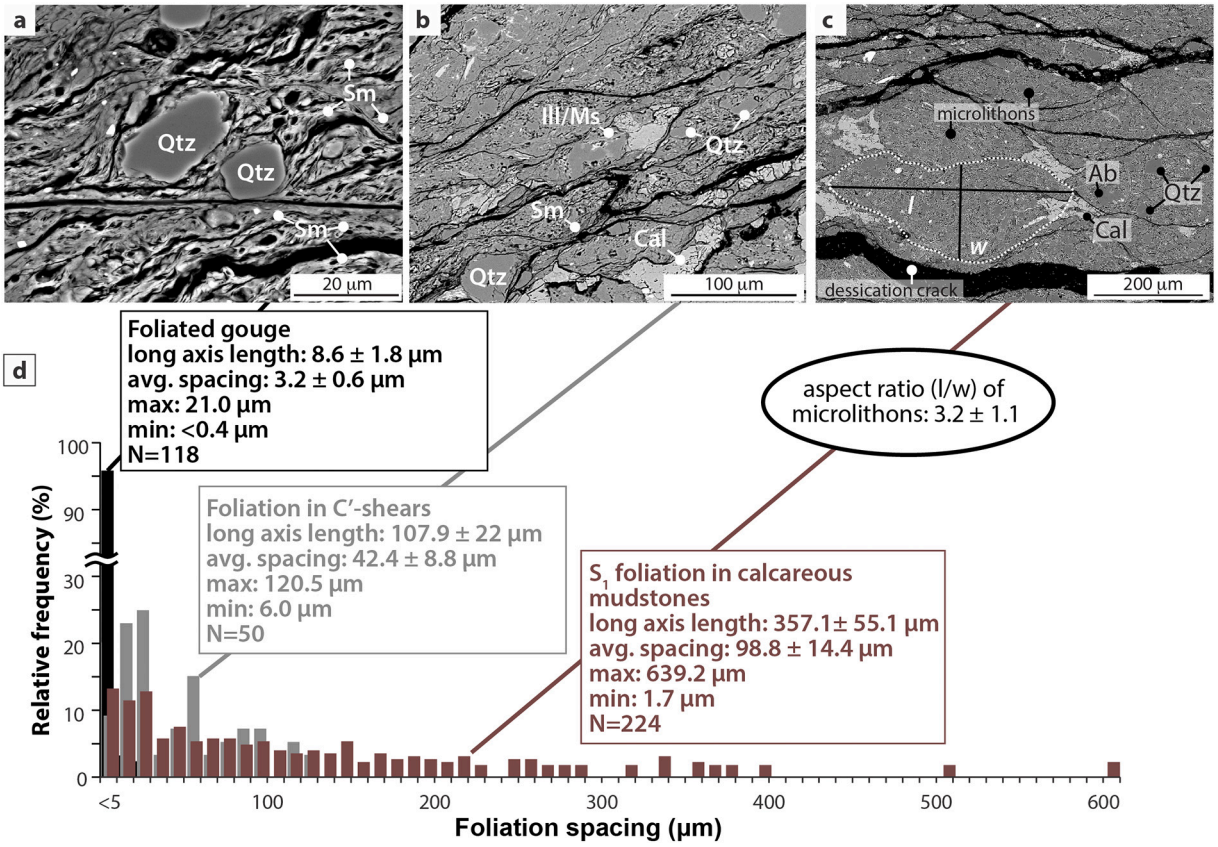

Fig. 5. Foliation spacing analysis. (a) Backscatter electron (BSE) image of foliated gouge in a cross-cutting fault (HFZ16.8 m). (b) BSE image of foliated clay minerals in a C′-shear (HFZ5.75 m). (c) BSE image of a calcareous mudstone layer (HFZ2.7 m), showing sites between microlithons infilled with authigenic calcite. The aspect ratio (length (l)/width (w)) of a microlithon is illustrated. (d) Histogram of foliation spacing measurements in foliated gouge (black), C′ shears (grey) and calcareous mudstones (red-grey) across the Hungaroa fault core. Binning is 10 µm; errors are 95% confidence levels; mineral abbreviations as per Fig. 4. (For interpretation of the references to colour in this figure legend, the reader is referred to the web version of this article.)

relative proportions of phyllosilicate and tectosilicate minerals (cf., Table 1). Increases in the amount of quartz±plagioclase within the calcareous mudstones are observed to correlate with an increase in the foliation spacing (to >40 µm) and the density of fractures within and between microlithons (Figs. 4f, 5c). Although fractures within the microlithons are open or partially sealed with calcite, the regions between microlithons, commonly called boudin necks, are sealed by calcite veins with elongate blocky and stretched calcite fibers (Fig. 4f). This crystal habit has been associated with incremental shearing and dissolution-precipitation creep (Bons, 2001; Bons et al., 2012). The average aspect ratio of the microlithons is 3.2 ± 1.1 (1 s.d.) (Fig. 5c, d).

4.4. Microstructural descriptions of fault core calcite

Evidence for calcite solution transfer is ubiquitous in the fault core. Calcite has undergone the following processes during deformation: dissolution along stylolites and at the margins of clasts, veins, and microfossils; precipitation in foliation-parallel and foliation-perpendicular extension veins; precipitation in hybrid (shear + extension) veins along clast margins and C'-shears; and precipitation in strain fringes (Figs. 4 and 6). Calcite vein orientation correlates with the relative competence of the host rock, where competent rocks are defined as those with a relatively high yield strength (Fagereng et al., 2010; Fagereng and Beall, 2021) (Fig. 6). In calcareous mudstones, calcite veins are typically arranged parallel to the foliation, whereas in competent clasts they are disposed at a high angle (30–90°) to the foliation (Fig. 4c). In addition, where there is a marked competency contrast, such as at dilatational sites adjacent to clasts and between microlithons, calcite veins are most commonly arranged at a low (5–30°) angle to the foliation (Fig. 4d and f).

Calcite veins oriented parallel to the S_1 (mélange) foliation are discontinuous, with lengths ranging from 1 mm to 10 cm in the slip-parallel direction (Figs. 4b and 6a–d). Calcite in this orientation is inferred to have precipitated within extensional fractures that are locally observed to follow the anastomosing foliation (Fig. 6a). The foliation-parallel extensional calcite veins can contain wall-rock inclusions (Fig. 6a and d). Where these veins occur along the margins of competent clasts, they form sheets of slickenfibers, recording episodic calcite precipitation (Fig. 6d; see also 8c). Calcite crystals in foliation-parallel veins have blocky, elongate blocky and/or stretched habits; the term stretched is used to describe calcite crystals with a length to width ratio on the order of 100:1 (Fig. 6a and d) (terminology of Bons et al., 2012). Following precipitation, calcite dissolution occurred, yielding embayed vein margins and stylolites that are coated with residual clay minerals, quartz, oxides, and fragments of calcite (Fig. 6b and c; see also Fig. 4g).

Calcite veins oriented at low (5–30°) angles to the S_1 foliation and/or along the C'-shears are inferred to have infilled fractures that formed through a combination of dilatation and shear displacement (e.g., Fig. 4g). Calcite within the low-angle veins commonly has a blocky and/or elongated blocky habit, with individual crystals containing twin lamellae (Fig. 6d). Calcite precipitated between microlithons (in boudin necks) most commonly exhibits an elongated blocky habit (Fig. 4f) and is rarely twinned. As seen in the foliation-parallel veins, calcite veins oriented at low angles to the foliation contain stylolites (Fig. 6d). Calcite veins oriented at higher angles (30–90°) to the S_1 foliation occur within clasts (hereafter termed high-angle veins) (Fig. 6d–g). These clasts may contain multiple generations of calcite veins (Fig. 6e), and the veins commonly have crack-seal textures defined by wall-rock inclusion bands

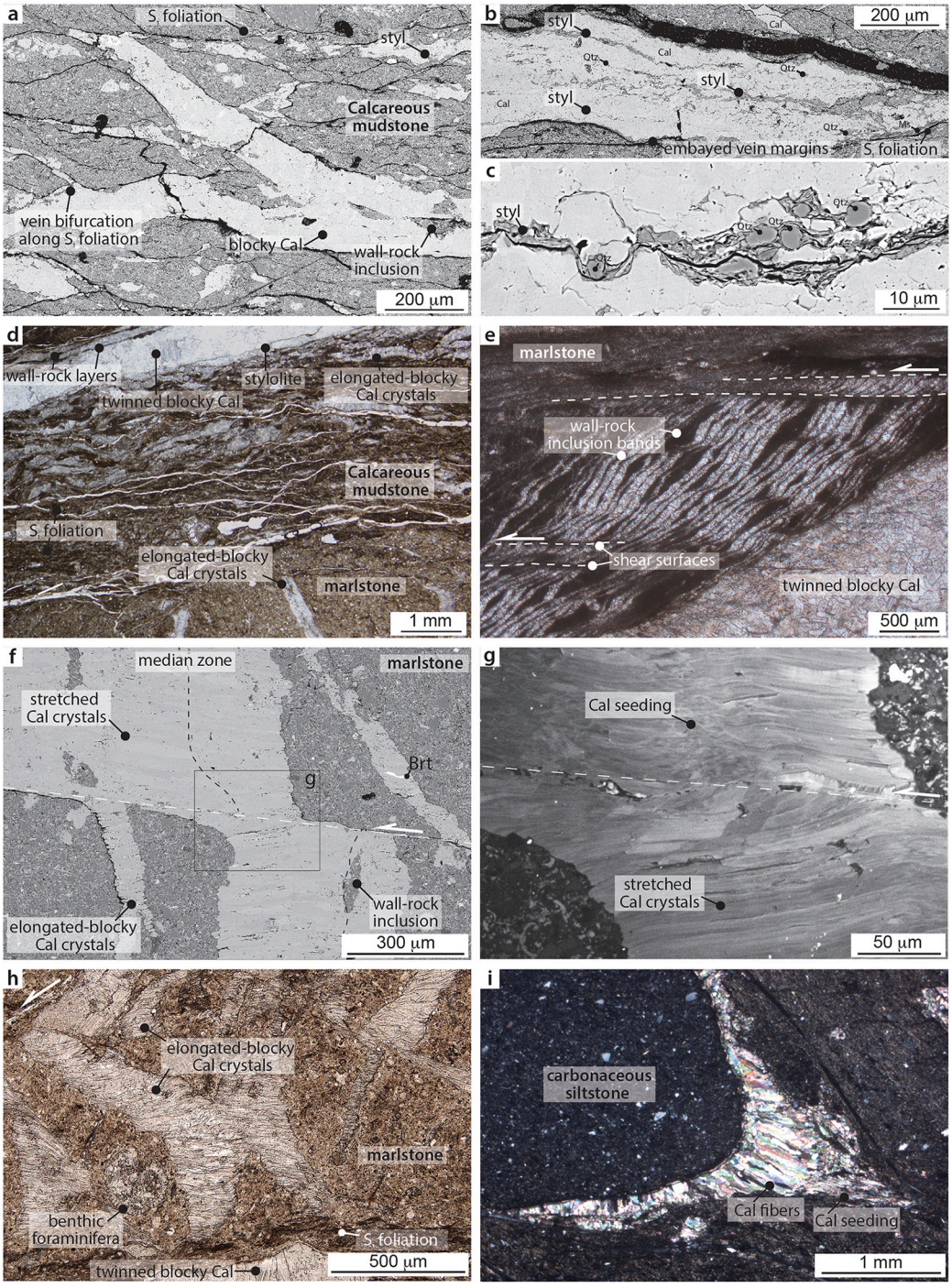

Fig. 6. Fault core calcite images. (a) BSE image of bifurcating S_1 foliation-parallel calcite vein (HFZ7.4 m). (b-c) BSE images of passive enrichment of quartz and phyllosilicates in stylolites oriented subparallel to the anastomosing S_1-foliation (HFZ7.4 m). (d) Plane polarized light (PPL) image of twinned, blocky calcite crystals in veins oriented at a low angle to the S_1-foliation and separated by wall-rock layers (upper left). Elongated-blocky calcite crystals occur in S_1-parallel veins (upper right). Older S_1-parallel veins have undulating to cuspate margins and are cross-cut by the anastomosing S_1 planes (center). Calcite veins forming a high angle with the S_1 foliation occur in a marlstone clast (lower center) (HFZ19.5 m). (e) PPL image of calcite-filled veins and inclusion bands formed by movement on slip surfaces transecting the edge of a marlstone clast (HFZ4.8 m). (f) BSE image of a shear fracture displacing high-angle calcite veins in a marlstone clast, with inset box showing the location of (g), a SEM cathodoluminescence image of median zone elongated-blocky calcite crystals transitioning to stretched crystals (HFZ2.7 m). (h) PPL image of a marlstone clast with an X-type calcite vein (cf. Arslan et al., 2008) recording the interaction between slip on the S_1 foliation (bottom) and movement on a shear fracture (upper left) (HFZ19.5 m). (i) Cross-polarized light (XPL) image of calcite-filled pressure fringe developed on a carbonaceous siltstone clast (HFZ3.2 m). Top-to-the-left shear sense in all figures; mineral abbreviations as per Fig. 4.

with <0.1 to 2 mm spacings (Fig. 6e). Crystal habit varies from blocky to elongate blocky, with veins oriented at the highest angles to the S_1 foliation having stretched crystals (Fig. 6f, g). Locally, the high-angle calcite veins have experienced dissolution and displacement along fractures (Fig. 6f–h).

Strain fringes filled with calcite occur adjacent to rigid clasts of carbonaceous sandstone and siltstone embedded within the sheared calcareous mudstone matrix (Fig. 6i). Calcite within the strain fringes has a habit that ranges from elongate blocky to fibrous. The long axes of the calcite fibers are oriented parallel to the anastomosing S_1 foliation. The long axes of the clasts and their trailing strain fringes display a sinistral obliquity to the foliation. Within the fault core sedimentary rocks, calcareous microfossils can be un-deformed, have partially dissolved margins, or contain thin (<30 µm-wide) internal stylolites (Figs. 4f and 6h). Locally, the calcareous microfossils are crosscut by brittle fractures and calcite veins.

5. Constraints on deformation conditions

5.1. Analytical methods—calcite isotopic analyses

Stable and clumped isotopes analyses were performed on 25 calcite veins (low-angle, high-angle, and foliation-parallel veins) and two host sedimentary rocks (micrite and marlstone) with 8 to 23 aliquots per sample (Table S1.9). Analyses were performed on powders (per aliquot 75 to 95 µg for the 253Plus and 130 to 160 µg for the MAT253) collected

from variably oriented calcite veins. Powders were extracted using a microdrill by New Wave Research with a tungsten carbide drill bit (300 μm in diameter). Larger samples were powdered with mortar and pestle. All powders were analysed using Thermo Scientific MAT253 and 253Plus isotope ratio mass spectrometers both connected to a Kiel-IV carbonate device following methods described in Meckler et al. (2014). Stable isotope results are reported in the conventional δ notation with respect to the Vienna Pee Dee Belemnite (VPDB) for calcite $\delta^{13}C$ and $\delta^{18}O$.

Clumped isotope results are expressed as Δ_{47} in the I-CDES reference frame (Bernasconi et al., 2021), with the per mil enrichment of $^{13}C^{18}O^{16}O$ in CO_2 released via phosphoric acid digestion of the carbonate relative to the amount expected for a random distribution of isotopes among all CO_2 isotopologues. Carbonate clumped isotope thermometry is based on the thermodynamically dependent abundance of ^{13}C—^{18}O bonds in the calcite lattice; importantly, this abundance is independent of assumptions about the fluid source $\delta^{18}O$ (Ghosh et al., 2006). Application of the Δ_{47}-temperature calibration of Anderson et al. (2021), based on carbonates formed at a wide temperature range, yields an estimate of calcite formation temperature. Combining the measured calcite $\delta^{18}O$ data with the temperature-dependent water-calcite oxygen isotope fractionation factors of O'Neil et al. (1969) and Kim and O'Neil (1997) then allows determination of the $\delta^{18}O$ of the fluid source ($\delta^{18}O_{fluid}$ relative to VSMOW) (complete methods in Supporting Information S1.7, S1.8). All uncertainties in the isotopic analyses are reported at the 95% confidence level.

5.2. Stable isotope results

The two host rock calcite samples yielded $\delta^{13}C$ values of +0.66 ± 0.13‰ and + 1.23 ± 0.03‰ and $\delta^{18}O$ values of −4.34 ± 0.26‰ and −4.66 ± 0.07‰ (Table S1.8) (Fig. 7a). Fault core calcite veins show a range of $\delta^{13}C$ values between +0.40 ± 0.07‰ and +1.52 ± 0.14‰, similar to the host rocks. However, the $\delta^{18}O$ values in the fault core calcite veins, between −6.02 ± 0.20‰ and −8.97 ± 0.26‰, are lower than the host rocks. Neglecting an outlier contaminated with host rock during microdrilling (HFZ35.3 m), fault core calcite mineralization is characterized by an average $\delta^{18}O$ value of −7.50 ± 0.26‰ ($N = 23$). A hanging wall (Mangapokia Formation) calcite vein that occurs within carbonaceous sandstone shows a $\delta^{13}C$ value of −2.43 ± 0.04‰ and a $\delta^{18}O$ value of −9.37 ± 0.08‰.

5.3. Clumped isotope thermometry and paleofluid $\delta^{18}O$ results

Clumped-isotope data from the fault core veins yield a narrow range of Δ_{47} values between 0.445 ± 0.024‰ and 0.482 ± 0.013‰, and this range is distinct from the Δ_{47} values measured in two host rock samples, 0.537 ± 0.021‰ and 0.551 ± 0.021‰ (Table S1.8) (Fig. 7b). Using the Δ_{47}-calibration equation of Anderson et al. (2021), these values correspond to fault core calcite vein precipitation temperatures between 71^{+9}_{-8} °C and 92^{+16}_{-14} °C (Fig. 7c), with an average precipitation temperature of 82^{+13}_{-12} °C. The hanging wall calcite vein Δ_{47}-temperature of 81^{+9}_{-9} °C lies within the same temperature range as the fault core veins.

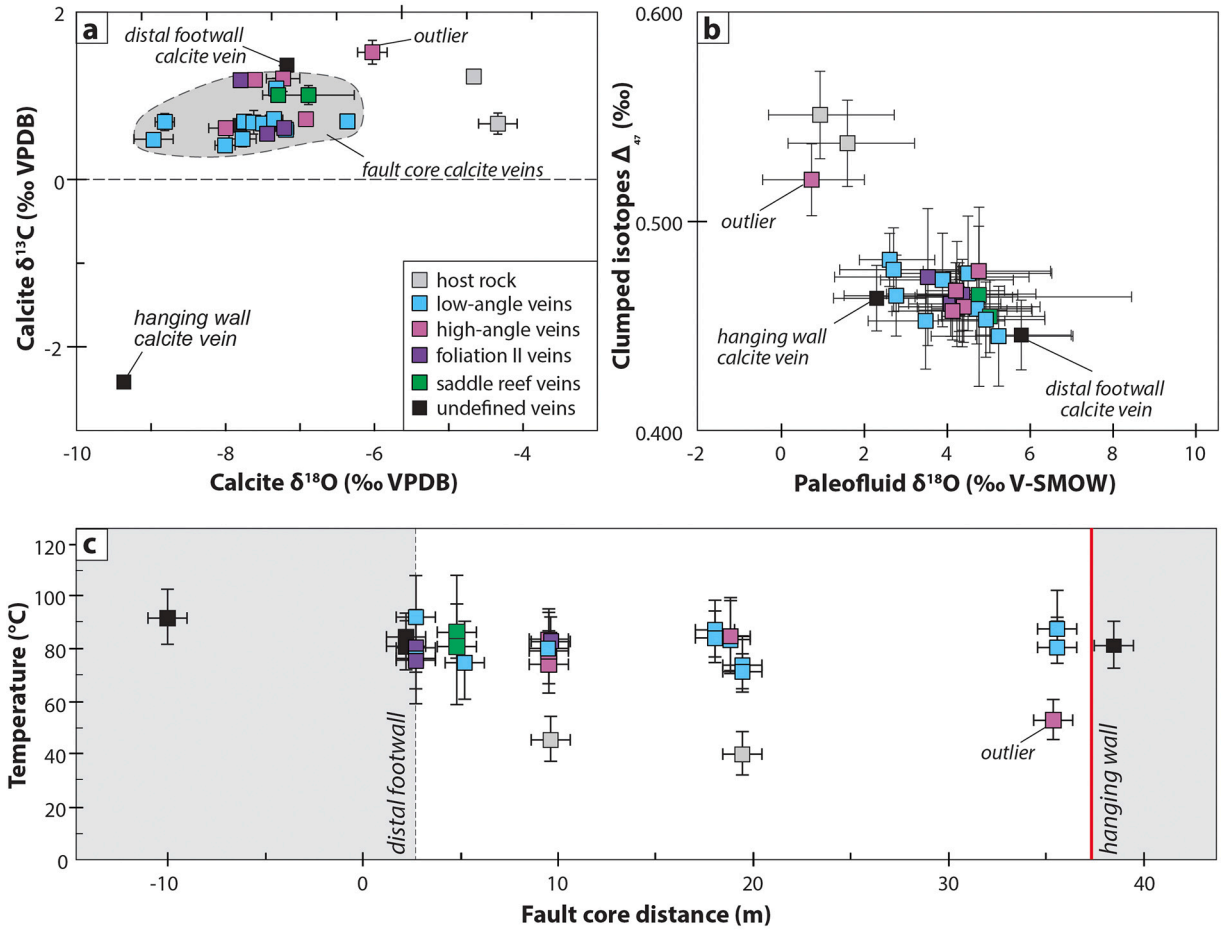

Fig. 7. Isotopic analyses. (a) $\delta^{13}C$ (‰ VPDB) versus $\delta^{18}O$ (‰ VPDB) diagram for the analysed calcite domains. Within the fault core, calcite vein $\delta^{18}O$ is depleted relative to host rocks. Legend applies to all plots. (b) Clumped isotope (Δ_{47}) values plotted against calculated fluid source $\delta^{18}O$ values. (c) Calcite precipitation temperatures derived from Δ_{47} measurements as a function of structural position. The x-axis is distance along the measured section, with an uncertainty of ±0.1 m. In (a-c), error bars indicate 95% confidence level.

Calculated using the clumped isotope temperature constraints, the fault core vein calcites' paleofluid source had $\delta^{18}O$ values between $2.6^{+1.1}_{-0.7}$‰ and $5.8^{+1.2}_{-1.1}$‰ (Kim and O'Neil, 1997; O'Neil et al., 1969). The Δ_{47}-temperatures and paleofluid $\delta^{18}O$ values of the fault core vein calcite are significantly different to the host rock calcites' Δ_{47}-temperatures, 40^{+9}_{-8} °C and 45^{+9}_{-8} °C, and paleofluid $\delta^{18}O$ values, $1.6^{+1.6}_{-1.4}$‰ and $0.9^{+1.8}_{-1.2}$‰. Given measurement uncertainties, the paleofluid $\delta^{18}O$ value calculated for the hanging wall calcite vein, $2.3^{+1.2}_{-1.0}$‰, overlaps with the fault core calcite veins.

6. Constraints on fault strength

6.1. Calcite paleopiezometry analytical methods

There are two main methods used to estimate the strength of exhumed fault zones: paleostress analysis (paleopiezometry) and extrapolation of experimentally determined flow laws for the strength of fault rocks (e.g., Behr and Platt, 2014; Collettini et al., 2019). Paleostress analyses in this study are based on twinning in calcite grains, specifically e-twin morphology, twin density, and twin orientations in syntectonically emplaced calcite veins. Analysed calcite veins comprise (1) foliation-parallel, (2) slickenfiber, (3) low-angle, (4) high-angle, and (5)

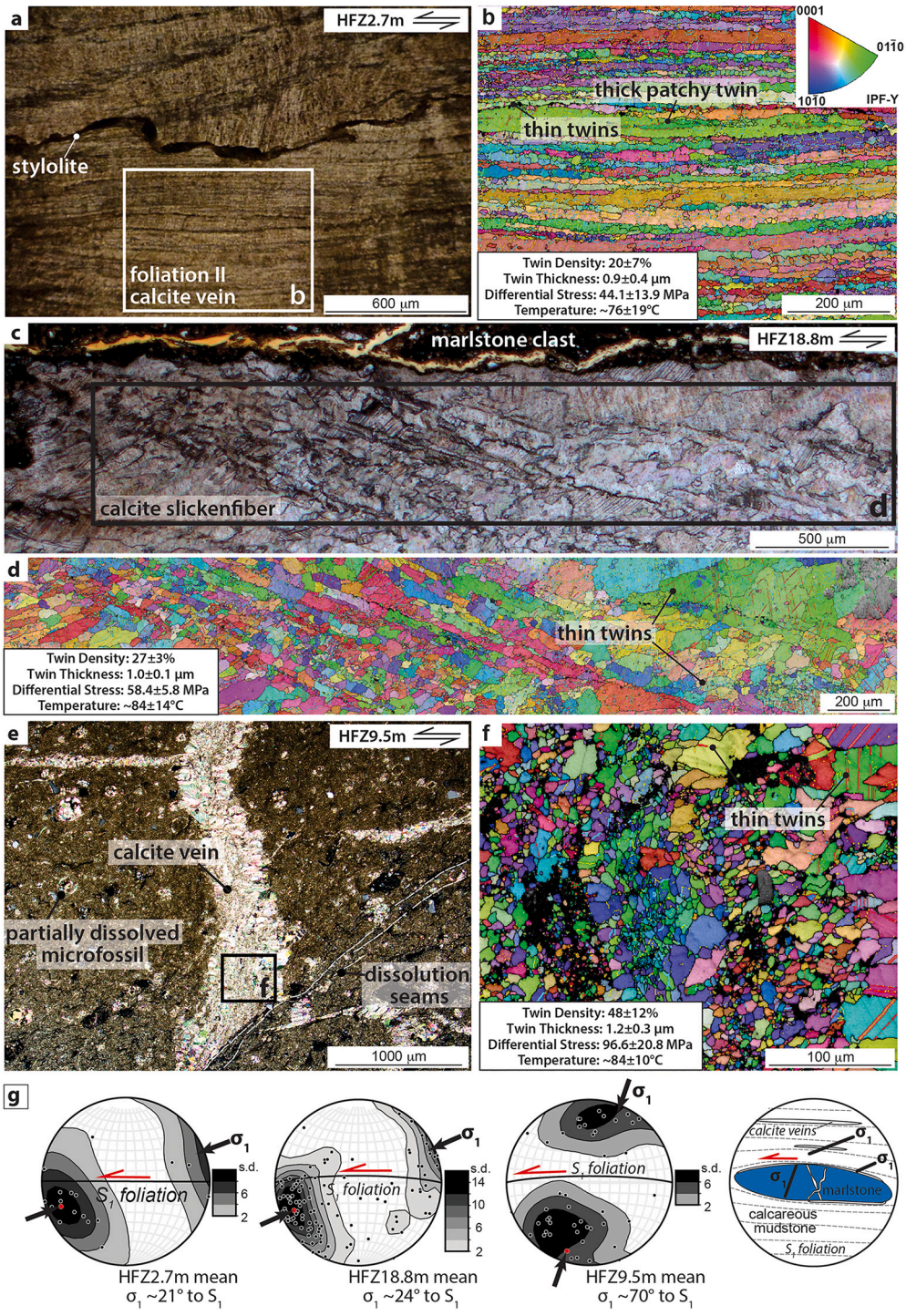

Fig. 8. Microphotographs and EBSD-based analyses of intracrystalline deformation in calcite veins. Temperature estimates are based on clumped-isotope thermometry of the same vein; differential stresses are based on twin densities following Ferrill (1998). Uncertainties are stated as 95% CL. (a) Stretched calcite crystals within a foliation-parallel vein, sheared calcareous mudstone (HFZ2.7 m). (b) EBSD-based orientation map of the stretched calcite crystals in (a). Inverse pole figure (IPF) crystal reference frame used to produce EBSD-based orientation maps (inset). Elsewhere, a differential stress of 79.2 ± 20.0 was measured in this vein (Table S1.5). (c) Calcite slickenfibers on a marlstone clast margin (HFZ18.8 m). (d) EBSD-based orientation map of blocky to elongate blocky calcite crystals of the analysed calcite slickenfibers in (c). (e) Extensional vein in a marlstone clast (HFZ9.5 m). (f) EBSD-based orientation map of the analysed blocky calcite crystals in the extensional vein of (e). (g) Lower hemisphere, equal area stereograms of contoured σ_1-directions based on Turner compressive stress axes calculated for each twin set (Evans and Groshong Jr, 1994; Turner, 1953) of the analysed calcite vein samples in (b), (d), (f) (L-R). Stress solutions are plotted in the kinematic XZ section relative to S_1 foliation (rotated to strike E-W). Also shown is an interpretative sketch of the σ_1 orientations in a calcareous mudstone containing a marlstone clast (kinematic XZ section).

saddle reef veins. Differential stresses based on calcite twin density are estimated using the paleopiezometers of Rybacki et al. (2013) and Ferrill (1998) (complete methods in Supporting Information S1.5).

6.2. Calcite paleopiezometry results

Based on optical microscopy, twins in calcite grains are approximately 1 μm-wide and straight throughout all calcite vein samples, resembling Type I twins of Burkhard (1993) and suggestive of deformation temperatures of <170 °C (Evans and Dunne, 1991; Ferrill et al., 2004). Based on EBSD analysis (Fig. 8), calcite twin thicknesses range from 0.8 ± 0.2 μm (HFZ5.2 m_1_a1; low-angle vein) up to 1.9 ± 0.3 μm (HFZ2.7 m_1_a2; foliation-parallel vein) with an average of 1.2 ± 0.3 μm (95% CL) across all analysed samples, also indicative of low deformation temperatures (<170 °C; Evans and Dunne, 1991; Ferrill et al., 2004).

Twin densities across all calcite vein samples range from 20 ± 7 twinsmm^{-1} (HFZ2.7 m_1_a3; foliation-parallel vein) to 48 ± 12 twinsmm^{-1} (HFZ9.5m_3_a3; high-angle vein), with an average of 35 ± 7 twinsmm^{-1} (95% CL). The estimated twin densities are independent of the size of the calcite grain hosting the twins (Table S1.5). Differential stresses estimates derived from twin densities range from 44.1 ± 13.9 MPa and 79.9 ± 20.0 MPa (Fig. 8a, b; foliation-parallel vein) and 58.4 ± 5.8 MPa (Fig. 8c, d; calcite slickenfiber vein) to 96.6 ± 20.8 MPa (Fig. 8e, f; high-angle vein). On the other hand, calcite-filled strain fringes and calcite between microlithons rarely contain twins, indicating low differential stresses (cf. Fig. 6i) (Lacombe et al., 2021).

Using the EBSD-based methods documented in Mizera et al. (2021), paleostress analyses of calcite e-twin orientation measured in a foliation-parallel vein (Fig. 8a, b) and a calcite slickenfiber (Fig. 8c, d) indicate that the maximum principal stress (σ_1) was oriented at a low angle (~21–24°) to the S_1 foliation (Fig. 8g). By contrast, analysis of calcite twin orientation in a high-angle calcite vein (Fig. 8e, f) indicates that the σ_1 direction was at high angle (~70°) to the S_1-foliation (Fig. 8g). These results complement our observations of extension veins having formed at both low and high angles to the foliation (e.g., Fig. 6) and are consistent with previously modelled spatial variations in the σ_1 direction within mélanges (Webber et al., 2018).

6.3. Hydrothermal friction experiments methods

To measure the frictional strength of Hungaroa fault core rocks, samples of a green-grey calcareous mudstone (HFZ3.7 m), a dark grey calcareous mudstone (HFZ5.2 m), and a micrite clast (HFZ9.6 m) were deformed in a ring shear apparatus adopting the methods described in Niemeijer et al. (2008) and den Hartog et al. (2012). Following Boulton et al. (2019), disaggregated samples were milled for 5 min in a McCrone mill to obtain starting materials with a grain size <10 μm. Experimental faults were created by placing a ~1 mm-thick sample layer between two pistons. The sample assembly was then loaded into an internally heated pressure vessel, saturated with deionised water, and allowed to consolidate for ~30 min under a set temperature (T = 40 °C or 120 °C) and effective normal stress (σ_n') of 60 MPa (100 MPa total applied load, less 40 MPa pore fluid pressure, equivalent to a pore fluid factor, λ, of 0.4).

A servo-controlled electromotor sheared the experimental faults in two stages: sliding to displacements >10 mm took place at a velocity (V) of 0.3 μm/s to establish a steady-state coefficient of friction (μ_{ss}) (hereafter termed the friction coefficient) and microstructure, followed by a series of 10 velocity steps alternating between 0.3 and 1 μm/s (an up-step) and 1 and 0.3 μm/s (a down-step) to measure the friction coefficient, the friction rate parameter (a–b), and their standard deviations. An iterative least-squares method incorporating the Dieterich (1979) rate-and-state friction equations was used to quantify the friction rate parameter (a–b), which at steady-state is defined as the logarithmic velocity dependence of friction following:

$$(a-b) = \frac{\partial \mu_{ss}}{\partial \ln V} \quad (1)$$

According to rate-and-state friction theory, rocks that exhibit positive values of (a–b) are prone to aseismic creep because they are intrinsically stable and rate-strengthening (Scholz, 1998; Marone, 1998). A rock that exhibits negative values of (a–b) is rate-weakening and can nucleate a frictional instability if the elastic stiffness (k) of the loading system (i.e., the fault and its wall rocks) is smaller than a critical stiffness (k_c), which is defined by the frictional properties of the slipping fault (Ruina, 1983; Scholz, 1998) (complete methods in Supporting Information S1.9).

6.4. Hydrothermal friction experiments results

Hydrothermal friction experiments were performed on fault core samples that contain varying proportions of quartz, calcite, phyllosilicates, and trace amounts of plagioclase and accessory minerals (Table 1). At T = 40 °C, calcareous mudstone samples HFZ5.2 m and HFZ3.7 m have friction coefficients of 0.40 and 0.42, respectively. However, the micrite sample HFZ9.6 m exhibits a higher μ_{ss} of 0.64 at T = 40 °C (Fig. 9a). Friction coefficients also correlate with calcite content at T = 120 °C, increasing from μ_{ss} = 0.38 (HFZ5.2 m) to μ_{ss} = 0.50 (HFZ3.7 m) and μ_{ss} = 0.61 (HFZ9.6 m) (Table 2) (Fig. 9b). In velocity-stepping experiments, the calcareous mudstone samples (HFZ5.2 m and HFZ3.7 m) have positive values of (a–b) at temperatures of 40 °C and 120 °C. In contrast, the frictionally stronger micrite sample (HFZ9.6 m) is rate-weakening and exhibits negative values of (a–b) at both T = 40 °C and 120 °C, undergoing stick-slip instabilities throughout the higher temperature experiment (Table 2) (Fig. 9). Whereas the frictionally weaker, rate-strengthening calcareous mudstones form the pervasively sheared matrix of the fault core, the frictionally stronger and rate-weakening micrite only occurs as spatially dispersed clasts (cf. Fig. 3) (Sections 3 and 4). Estimates of fault strength obtained from the hydrothermal friction experiments are compared with differential stress estimates obtained from paleopiezometry in Section 7.2.

7. Discussion

7.1. Deformation history

A deformation history of the Hungaroa fault can be deduced using regional mapping observations, field observations, microstructural descriptions, and published tectonic reconstructions (Figs. 1-3) (this study; Nicol et al., 2007; Furlong and Kamp, 2009; Lamb, 2011; Hines et al., 2013). Following deposition of Cretaceous to Eocene sedimentary rocks, deformation resulted in: (1) the development of asymmetric folds in bedding (S_0) that became more tightly appressed eastward towards the fault core, a fold geometry that reflects increasing strain towards the fault (Fig. 2). Within the ~33 m-wide fault core, (2) the asymmetric folds were transposed into isoclinal structures, and S_0 was disrupted into lenticular or sigmoidal clasts (phacoids). In addition, shearing of the calcareous mudstones formed a tectonic foliation (S_1) that anastomoses around phacoids (Figs. 2, 3), which is (3) locally cross-cut and deflected by oblique C′-shears (Figs. 2d, 3c, 4a, b, g). Sliding on the S_1 foliation and C′-shears was accompanied by abundant calcite dissolution and (re) precipitation (Figs. 4f, 6), and an overall sinistral fabric asymmetry developed (Figs. 3c, 4a, b). Later, (4) discrete, gouge-bearing faults subparallel to the Hungaroa fault sharply cut across the shear fabrics (Figs. 2e, 3b, 4h–j). Finally, (5) rotation of the now-inactive Hungaroa fault zone took place on the western limb of the younger regional Coastal Anticline (Fig. 1) (Hines et al., 2013).

The Middle to Late Eocene Wanstead Formation is the youngest stratigraphic unit displaced by the Hungaroa fault zone, and it forms the matrix of the fault core (Figs. 1–3). Slip on the fault must post-date deposition of the Wanstead Formation, but there are no further

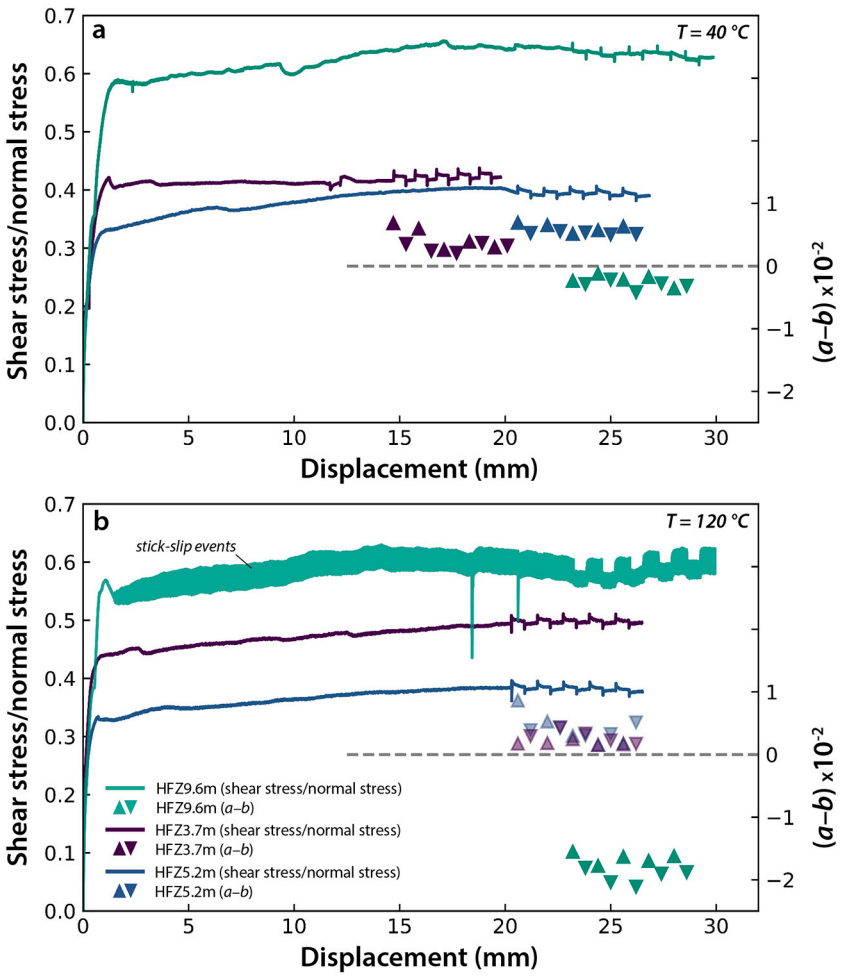

Fig. 9. Hydrothermal friction experiments performed on samples HFZ5.2 m (32% calcite, 37% phyllosilicates), HFZ3.7 m (56% calcite, 27% phyllosilicates), and HFZ9.6 m (78% calcite, 8% phyllosilicates). (a) Plot of the coefficient of friction (μ = shear stress/normal stress, assuming no cohesion) against displacement for experiments performed at $T = 40$ °C. Dashed line at Y2 = 0 divides the (a–b) >0, rate-strengthening, data from the (a–b) <0, rate-weakening, data. (b) Plot of the coefficient of friction against displacement for experiments performed at $T = 120$ °C. Legend in (b) applies to both plots. Upwards facing triangles denote velocity up-steps and downwards facing triangles denote velocity down-steps.

Table 2
Summary of hydrothermal friction experiment results. Column heading abbreviations are: temperature (T); effective normal stress (σ_n'); steady-state coefficient of friction (μ_{ss}); the friction rate parameter (a–b); standard deviation (std. dev.).

Experiment	Sample	T (°C)	σ_n' (MPa)	μ_{ss}*	μ_{ss} std.dev.	(a–b) upstep	(a–b) std.dev.	(a–b) downstep	(a–b) std.dev.
u766	HFZ3.7 m	40	60	0.42	0.0018	0.0061	0.00069	0.0053	0.00020
u767	HFZ5.2 m	40	60	0.40	0.0016	0.0045	0.0019	0.0030	0.00070
u768	HFZ3.7 m	120	60	0.50	0.0025	0.0040	0.0029	0.0039	0.00085
u769	HFZ5.2 m	120	60	0.38	0.0020	0.0018	0.00037	0.0029	0.0010
u955	HFZ9.6 m	40	60	0.64	0.0047	−0.0022	0.00087	−0.0030	0.00074
u956	HFZ9.6 m	120	60	0.61	0.0087	−0.017	0.00085	−0.020	0.0012

* Steady-state friction coefficient reported as the mean of the initial friction (μ = shear stress/normal stress, assuming no cohesion) at each of the 5 velocity up-steps.

(younger) stratigraphic constraints on the timing of fault slip. Additional information is available from the fault core fabric and hanging wall/footwall age relationships, which indicate sinistral-reverse kinematics in the present-day coordinates. Sinistral slip on a NE-striking subvertical fault is incompatible with the present-day plate convergence vector and tectonic setting. Therefore, the deformation likely occurred during an earlier stage in the development of the HSM (Figs. 1a, 10) (Beavan et al., 2002). In the Early Miocene, significant amounts of margin-perpendicular shortening occurred along low-angle thrust faults within the East Coast Basin sequence (Chanier and Ferriere, 1991; Nicol et al., 2007; Rait et al., 1991). Later, folding within the (probably late Neogene) Coastal Anticline would have over-steepened the fault.

The original dip of the Hungaroa fault is unknown; however, because the fault parallels bedding in both its footwall and hanging wall, we infer it to have dipped at a low angle (≤10°) to the horizontal. Based on this inference, the fault dip and shearing directions were restored by rotating 67° about the modern strike of the Hungaroa fault (012°). This horizontal-axis rotation, which is anticlockwise when looking NE, restores the Hungaroa fault to a shallow dip of 10°ESE and places the older Mangapokia Formation structurally above the younger Wanstead Formation, as would be expected for a thrust fault (Fig. 10d) (Supporting Information S1.1). In this restored orientation, which is approximate, the gently dipping Hungaroa fault is a (landward-verging) back-thrust with top-towards-the WNW transport direction (Fig. 10d). Reconstructing the original geometry and kinematics of the Hungaroa fault would require an additional counterclockwise vertical-axis rotation of between 45° (Nicol et al., 2007) and 80° (Lamb, 2011) (Fig. 10d), but further age and paleomagnetic data are necessary to perform this restoration accurately.

On the Wairarapa Coast north of Tora, at Flat Point, a more complete sedimentary sequence enabled Chanier and Ferriere (1991) to show that movement on top-towards-the-SE (seaward-verging) thrust sheets

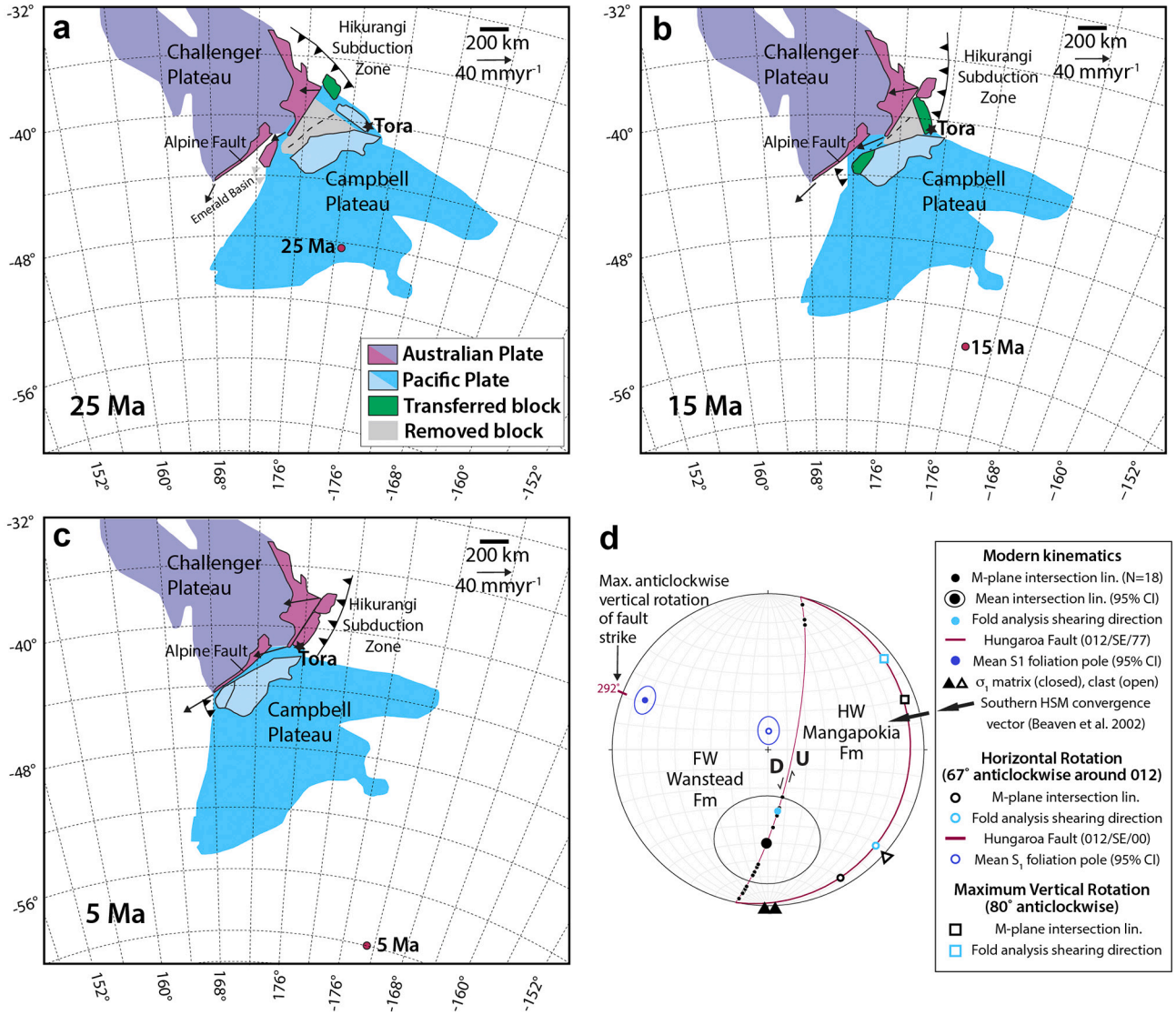

Fig. 10. Plate reconstructions showing inferred Neogene rigid-body vertical-axis rotation of the ECB, Tora, and Hungaroa fault. (a) Tectonic reconstruction of the Australian and Pacific Plates 25 Ma. Study area and pole of rotation denoted with a blue star and red circle, respectively. Subduction along the NW-SE trending HSM had commenced, with the Raukumara Peninsula (green block) being transferred to the Australian Plate. (b) At 15 Ma, the HSM trends NNE-SSW at 15 Ma; green shapes denote the Wairarapa block, North Island, and Fiordland block, South Island, which are being transferred to the Australian and Pacific Plates, respectively. (c) After additional clockwise rotation, the HSM trends NE-SW at 5 Ma. Figures (a-c) modified from Furlong and Kamp (2009). (d) Stereographic analysis of the Hungaroa fault and fault core fabric elements. Paired S_1-foliation and C′-shear poles define a movement (M) plane of shearing (cf. Fig. 2d); the mean M-plane intersection with the fault (black dot with 95% Cl ellipse) is a mean calculated shearing direction. See key and text for further fault restoration details. (For interpretation of the references to colour in this figure legend, the reader is referred to the web version of this article.)

occurred in the Early Miocene, a timing we favour for Hungaroa fault zone activity. Uplifted areas of the HSM contain multiple Early Miocene thrust sheets that localised in smectitic mudstones of the Wanstead Formation (Maison et al., 2018; Pettinga, 1982; Rait et al., 1991). Together, these structures accommodated tens of kilometres of shortening along the contracting margin, with tectonic windows indicating at least 10 km of displacement on some thrust sheets (Nicol et al., 2007; Rait et al., 1991). Yet movement along a low-angle thrust with an assumed dip $\leq 10^{\circ}$ would have required conditions of fault weakness (Hubbert and Rubey, 1959). We will now present constraints on the temperature and pressure conditions present at the time of faulting and then explore the extent to which the Hungaroa fault zone was weakened through pore fluid overpressures and/or fabric development.

7.2. *Deformation conditions*

7.2.1. *Fault core fluids, temperatures*

Determining the mechanisms responsible for tectonite development within the Hungaroa fault core requires estimates of the temperature and effective normal stress(es) during deformation. The spatial relationship between dilatational sites created by shearing on the S_1 foliation — such as boudin necks and strain fringes — and the calcite veins infilling them indicates that the latter have a syntectonic origin (Figs. 4f, 6) (e.g., Passchier and Trouw, 2005). Similarly, shearing along the S_1 foliation around clasts created space for calcite precipitation in slickenfiber veins (Fig. 8c, d) (e.g., Bons et al., 2012). A syntectonic origin for extensional calcite veins oriented at both low angles and high angles to the S_1 foliation is also likely, because they formed from fluid-driven hydrofracturing and/or locally high deviatoric stresses within the actively shearing mélange (Fagereng et al., 2018; Secor, 1965; Webber

et al., 2018). A causal relationship exists between compaction, thrust faulting, and pore fluid overpressure development in low-permeability rocks (Fig. 8g) (Faulkner et al., 2018; Sibson, 2017). Wanstead Formation smectitic mudstones, which comprise the fault core matrix, have very low permeabilities ($\leq 10^{-21}$ m^2 for 30% smectite, <35% porosity) and are responsible for pore fluid overpressures throughout the East Coast Basin (Burgreen-Chan et al., 2016). Porosity-filling calcite precipitation and foliation development subparallel to fault zone boundaries would further limit fluid egress (Saffer and Tobin, 2011), and both processes are observed within the Hungaroa fault core (Figs. 3, 4). Therefore, we infer that the Hungaroa fault core calcite veins formed contemporaneously with fault zone deformation and that the calcite precipitation temperatures reflect the temperature of deformation (e.g., Luetkemeyer et al., 2016).

Carbonate clumped isotope thermometry analyses were performed on 25 calcite veins collected from the HFZ distal footwall, fault core, and hanging wall, with a majority of the samples obtained from veins within the fault core. Regardless of orientation, the calcite veins formed at a narrow range of temperatures between 71^{+9}_{-8} °C and 92^{+16}_{-14} °C, with an average precipitation temperature of 82^{+13}_{-12} °C (Fig. 7c). Converting the temperature to a depth requires constraints on the geothermal gradient and paleo-surface temperature. For the North Island passive margin, pre-Oligocene geothermal gradients of 30 ± 2 °C/km (Jiao et al., 2014) and 27.5 ± 2.5 °C/km (Tippett and Kamp, 1993) are used in thermochronology literature. Similar geothermal gradients persisted until between 15 and 5 Ma, based on modern-day temperatures combined with vitrinite-inertinite reflectance and fluorescence, apatite fission track, thermal alteration index, and Rock-Eval T_{max} analyses of six petroleum wells across the ECB (Burgreen-Chan and Graham, 2018). Thus, neglecting shear heating, the calcite veins would have precipitated between 2 and 4 km depth. The ubiquitous presence of low-temperature montmorillonite within the calcareous mudstones and marlstones also points to deformation having taken place at low temperatures and shallow crustal levels (Table 1) (Colton-Bradley, 1987).

Geological, mineralogical, and isotopic evidence indicates that the Δ_{47} temperatures calculated from calcite veins are primary precipitation temperatures. However, research has shown that later exposure to higher or lower temperatures can cause solid state isotope reordering in calcite, leading to erroneous interpretations (e.g., Henkes et al., 2014; Stolper and Eiler, 2015). Combining solid state reordering models with possible burial scenarios shows that calcite precipitation at much higher temperatures, with a later lower temperature reordering overprint, is not theoretically possible (Hemmingway and Henkes, 2021; Stolper and Eiler, 2015). Vein calcite precipitation temperatures significantly lower than those indicated by the measured clumped isotope values would require subsequent burial depths and/or geothermal gradients that exceed plausible values (Burgreen-Chan and Graham, 2018; Field and Uruski, 1997; Jiao et al., 2014). Additionally, the host rock Δ_{47} temperatures are marginally higher than the paleo-surface water temperatures (~25 °C; Liu et al., 2009); since these samples were collected adjacent to higher-temperature calcite veins, wholesale solid state isotope reordering is unlikely (Fig. 7) (Table S1.8).

Combined with the precipitation temperatures, carbonate stable isotope results provide insight into the fault zone paleofluid source. At Tora, the Middle to Late Eocence Wanstead Formation, which forms the mélange matrix, was deposited in a marine environment at bathyal depths (>3500 m) (Hines et al., 2013). The calculated $\delta^{18}O$ paleofluid values of the host rock calcite are reasonably consistent with precipitation from seawater, and the vein calcite $\delta^{18}O$ paleofluid values are indicative of rock-exchanged diagenetic fluids (e.g., Huntington and Lechler, 2015) (Fig. 7b). Since fault core and footwall calcite vein $\delta^{13}C$ values (0.40 ± 0.07–1.52 ± 0.14‰; mean 0.81 ± 0.13‰) overlap with the host rocks (0.66 ± 0.13‰ and 1.23 ± 0.03‰), bicarbonate ions transported by the paleofluids were likely derived from host rock dissolution. Notably, the hanging wall vein collected from the carbonaceous Mangapokia Formation is significantly more depleted in $\delta^{13}C$ (−2.43 ± 0.04‰) (Fig. 7a). Determining paleofluid pathways and the effect(s) of the anisotropic fault core fabric on paleofluid flow remains the subject of current research.

7.2.2. Fault core stresses

Setting the vertical stress (σ_v) equal to the (applied) minimum principal stress (σ_3), consistent with an Andersonian thrust faulting regime, and assuming that the intermediate principle stress (σ_2) lay within the fault plane, allows us to perform a simple 2D stress analysis on the HFZ at 3 km depth (Fig. 11) (Sibson, 1985). The HFZ fault core comprises (dominantly) calcareous marlstone clasts within a sheared calcareous mudstone matrix (Figs. 2, 3, 4). To capture potential variations in differential stress, this lithological heterogeneity requires the evaluation of four different Mohr-Coulomb failure envelopes: (1) a representative sliding friction coefficient ($\mu = 0.40$) for the calcareous mudstone; (2) a representative sliding friction coefficient ($\mu = 0.60$) for the marlstone and micrite clasts; (3) a minimum sliding friction coefficient ($\mu = 0.11$) for an interconnected foliation of pure montmorillonite (Morrow et al., 2017); and (4) a maximum peak friction coefficient ($\mu = 0.70$) for pure calcite (Verberne et al., 2014). The chosen clast friction coefficient ($\mu = 0.60$) is slightly lower than the micrite friction coefficients measured experimentally; this choice reflects the proportionally higher amounts of weak phyllosilicates in marlstone, the most common clast type (Tables 1, 2). Conditions of hydrostatic pore fluid pressure ($\lambda = 0.4$) and sub-lithostatic pore fluid pressure ($\lambda = 0.9$) are evaluated, noting that any pore fluid pressure between hydrostatic and lithostatic is possible, with lithostatic pore fluid pressure driving hydrofracturing (Figs. 6, 8, 11) (Fagereng et al., 2018; Sibson, 2017).

Hydrofracturing requires pore fluid overpressures ($P_f > \sigma_3 + T$) and occurs at low differential stresses of (σ_1–σ_3) < 4T, where T is the (lithology-dependent) tensile strength (Figs. 4, 6) (Secor, 1965; Sibson, 2017). These conditions of extreme fault weakness would have been transient because hydrofractures create space, reducing pore fluid pressures. On the contrary, the calcite twin densities (Fig. 8) record the maximum differential stresses acting on the fault (Fig. 11) (e.g., Ferrill, 1998; Rybacki et al., 2013). Differential stress estimates obtained from calcite twin densities of 44.1 ± 13.9 MPa and 79.2 ± 20.0 MPa (Fig. 8b), 58.4 ± 5.8 MPa (Fig. 8d), and 96.6 ± 20.8 MPa (Fig. 8f) are consistent with differential stresses sustainable by an optimally oriented cohesionless fault at 3 km depth with a friction coefficient between 0.4 and 0.7 and hydrostatic pore fluid pressure, or a non-optimally oriented fault containing moderately overpressured fluids (Fig. 11) (Hubbert and Rubey, 1959).

The restored dip of the Hungaroa fault (~10°) and other early Miocene thrust sheets is too low for slip at the friction values measured experimentally with hydrostatically pressured fluids (Fig. 11) (e.g., Rait et al., 1991). Calcite twin-based stress inversions on matrix veins indicate that σ_1 was oriented ~20° from the foliation, making the foliation better oriented for slip than the fault plane itself (Fig. 8g). For a matrix friction coefficient of $\mu = 0.4$, modest — and commonly observed — pore fluid overpressures ($\lambda > \sim 0.5$) are required for slip on the foliation at differential stresses of ~46 MPa at 3 km depth (e.g., Saffer and Tobin, 2011). However, at $\lambda \sim 0.5$, higher differential stresses of ~68 MPa would be required to drive shear failure of the marlstone clasts, which have a higher friction coefficient of $\mu = 0.60$ and are assumed to be cohesionless (Figs. 6f, g, 9, 11) (eq. 6 in Sibson, 2009). In a homogeneously stressed fault core, frictional sliding along the weaker foliation would always occur at lower differential stresses than shear failure of the marlstone clasts, regardless of the pore fluid pressure (Fig. 11). To achieve differential stresses high enough to cause shear fractures in the marlstone clasts, the matrix must have undergone marked strengthening. Alternatively, the clasts and matrix experienced heterogeneous stress states.

Extension veins typically form orthogonal to the minimum principal stress (σ_3) at differential stresses less than four times the host rock's tensile strength, with the tensile strength of calcareous mudstones and

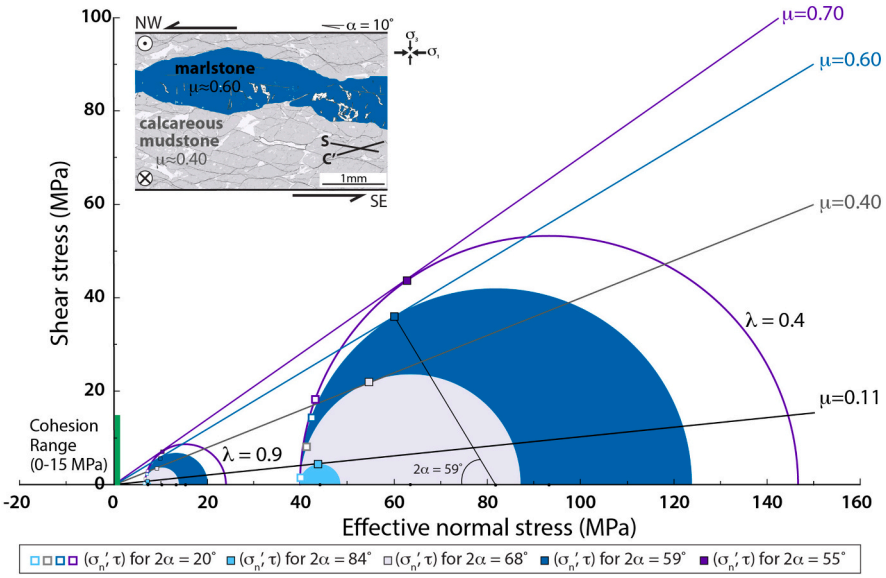

Fig. 11. 2D Mohr-Coulomb stress analysis. The cohesion of intact, porous limestone may be up to 15 MPa, with lower values expected for more clay-rich facies (Gharechelou et al., 2020; Renani and Martin, 2018). Mohr circles plotted assuming an overburden stress (σ_v) equal to the minimum principal stress (σ_3), a mean sediment density is 2250 kg/m^3, and pore fluid pressure (P_f) values given by pore fluid factors ($\lambda = P_f/\sigma_v$) of $\lambda = 0.4$ (hydrostatic) and $\lambda = 0.9$ (sub-lithostatic). For each friction coefficient, the values of shear stress (τ) and effective normal stress (σ_n') are plotted for a plane optimally oriented for slip (e.g., $2\alpha = 59°$ for $\mu = 0.60$) and for the horizontally rotated dip of the Hungaroa fault ($2\alpha = 20°$) (squares; see legend) (Sibson, 1985). Inset depicts HFZ restored kinematics and observed microstructures.

marls ranging between ~2 and 8 MPa (Ashtari et al., 2019; DeReuil et al., 2019; Gharechelou et al., 2020; Secor, 1965). In the HFZ, extension veins formed at low and high angles to the foliation, potentially reflecting stress rotations within the fault core (Fig. 6). Twins in matrix calcite veins record a σ_1 direction oriented ~20° to the foliation, but marlstone clast calcite vein twins record a σ_1 direction ~70° to the foliation (Fig. 8). Several explanations for variable stress orientations in mélanges have been proposed: (1) large-scale principal stress switching between vein formation events because of near-complete coseismic stress drops (Meneghini and Moore, 2007; Hasegawa et al., 2012); (2) force chains developing between "jammed" clasts (Beall et al., 2019; Webber et al., 2018); and (3) local stress risers arising from differences in clast/matrix particle velocities, with stress riser orientation and magnitude determined by clast and matrix properties as well as flow vorticity (Goodwin and Tikoff, 2002; Fagereng, 2013; Sibson, 2017; Fagereng and Beall, 2021).

Our datasets do not exclude the possibility that large-scale stress switching affected stress orientations within the fault core, which in turn influence resolved shear and normal stresses (Fig. 11). However, our observations of variations in σ_1 orientation *and* higher differential stresses within clasts and clast-rich regions make matrix-clast interactions (± matrix strengthening) the most likely explanation. Models of actively deforming mélanges confirm that clasts can experience shear stresses over 3 times greater than those felt by the matrix, even in unjammed states, with larger amplifications occurring in regions with jammed clasts (Beall et al., 2019). An additional discussion of the potential for matrix strengthening is presented below in Section 7.3.

Taken together, the Hungaroa fault core structures reflect spatio-temporal stress and strength heterogeneity – conditions expected for a tabular fault zone containing competent clasts embedded in an interconnected, rheologically weaker matrix (Fagereng and Beall, 2021). Multiple values of effective normal stress and shear stress may have existed in different places simultaneously within the ~33 m-wide fault core. Stress amplifications and rotations observed in clast calcite veins are interpreted to reflect loading by slip on the anastomosing S_1 foliation (Fig. 8). Within clasts, the mutually cross-cutting relationships between shear fractures and extension veins provide evidence for temporal fluctuations in shear strength resulting from fluid overpressure transients (Fig. 6f, g). These pore fluid overpressures formed hydrofractures (extension veins) that were incrementally sealed by calcite precipitated at low temperatures (<100 °C) from diagenetic fluids (e.g., Bons et al., 2012; Ujiie et al., 2018).

7.3. Deformation mechanisms

A salient question remains whether the Hungaroa fault zone was governed by a frictional rheology, where fault strength is a product of the effective normal stress and coefficient of friction, which has a small velocity dependence (Figs. 9, 11) (Dieterich, 1979; Scholz, 1998). At the strain rates imposed during (low-velocity) laboratory experiments, frictional sliding involves granular flow processes such as grain sliding, rotation and cataclasis, which involve dilatation and compaction (e.g., Niemeijer and Spiers, 2005). At laboratory strain rates, HFZ calcareous mudstones exhibit (sliding) friction coefficients between 0.38 and 0.50; a micrite has higher friction coefficients of 0.61 and 0.64 (Table 1). The friction coefficients measured are typical of Paleogene calcareous sediments recovered from the subducting Pacific plate at ODP Site 1124, with that site containing a ~3 m-thick interval of weaker smectitic sediments ($\mu = 0.16–0.28$ at $T \leq 150$ °C) (Boulton et al., 2019). However, direct extrapolation of experimental results to a natural fault zone that deformed at much lower geological strain rates would neglect observations indicating that viscous diffusive mass transfer (DMT) processes played a key role in accommodating HFZ deformation (Figs. 4, 6).

The common occurrence of embayed calcite grains (Fig. 4j), partially dissolved microfossils (Fig. 8e), opaque foliation-parallel seams of residual quartz and phyllosilicate minerals (Fig. 6d, e), and stylolites (Fig. 6b, c), reflects widespread, stress-driven, calcite dissolution within the fault core (Rutter, 1976). Calcite precipitation in low-stress sites between microlithons (Fig. 4d, f), along clast margins (Fig. 8c), in pressure fringes (Fig. 6i), and within extensional fractures (Figs. 4c, 6a, e, f) required calcite transport in a solution, a process called diffusion (Rutter, 1976). Diffusive mass transfer involves the serial steps of dissolution, diffusion, and precipitation of a soluble mineral (calcite) in a fluid phase (Rutter, 1976). Within the low-temperature HFZ, where calcite was highly soluble and there were ample precipitation sites, diffusion would have been the rate limiting process (Plummer and Busenberg, 1982; Zhang et al., 2010). The process of aseismic creep assisted by DMT and rate-limited by the diffusive flux (the diffusion coefficient multiplied by diffusion pathway thickness, length, and concentration gradient of the solute) is termed diffusion-controlled pressure solution creep (Bos and Spiers, 2002; Gratier et al., 2013). A fault zone deforming by diffusion-controlled pressure solution creep in parallel with frictional sliding has a frictional-viscous flow rheology (Bos and Spiers, 2002). At geological strain rates, where frictional sliding on a phyllosilicate foliation creates local stress (and chemical potential)

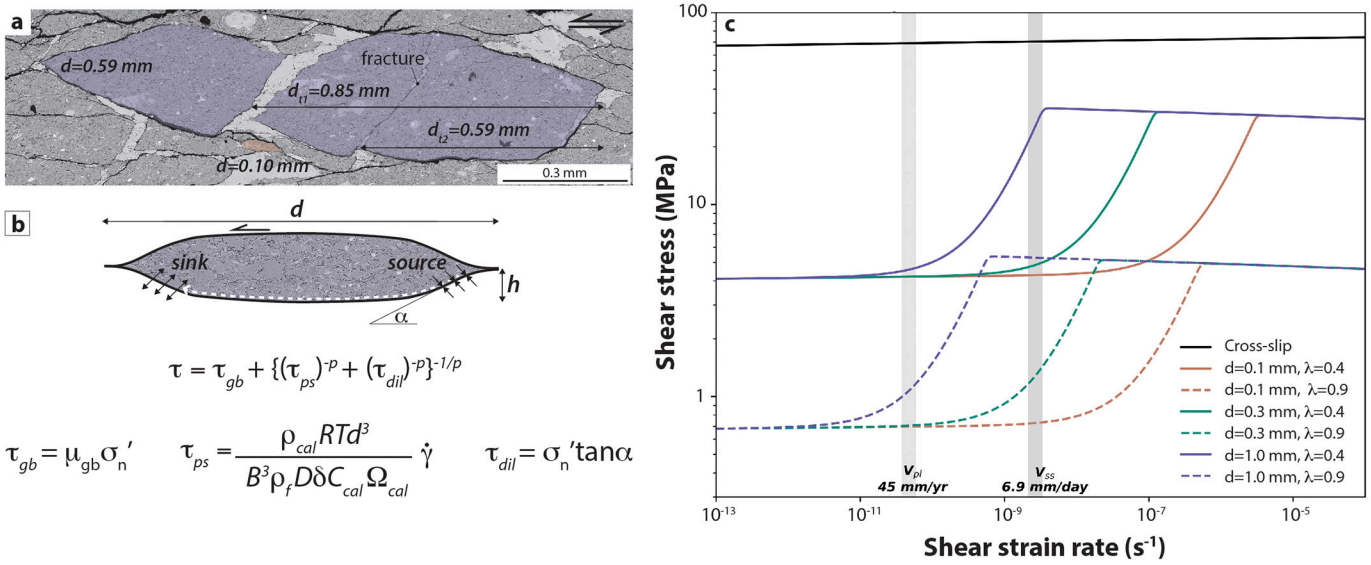

Fig. 12. Model of frictional-viscous flow in sheared calcareous mudstones comprising a fault core dipping 10° to σ_1 at 3 km depth. (a) Representative microstructures, showing calcite precipitated between microlithons; note the fracture in the largest microlithon, which reduces the diffusion length scale. (b) Microphysical model geometry and constitutive equations after Bos and Spiers (2002). Variables are: τ, total shear stress driving fault slip; τ_{gb}, shear stress required for frictional sliding; τ_{ps}, shear stress required to deform microlithons by diffusion-controlled pressure solution creep; p, an exponential factor (20); τ_{dil}, shear stress required for dilatation; ρ_{cal}, the density of calcite (2710 kgm^{-3}); R, the gas constant; T, absolute temperature (353.15 K); d, diffusion length scale (m); B, microlithon aspect ratio (3.2); ρ_f fluid density (1030 kgm^{-3}), D, diffusion coefficient of calcite (2.568^{-10} m^{3}s^{-1}) (Nakashima, 1995; Zhang et al., 2010); δ, fluid film thickness (10^{-8} m); C_{cal}, calcite solubility (1.186^{-5} m^{3}m^{-3}) (Plummer and Busenberg, 1982); Ω_{cal}, molar volume of calcite (3.692^{-5} m^{3}mol^{-1}). (c) Model results plotted as total shear stress required for slip against shear strain rate. Hikurangi Subduction Zone convergence (45 mmyr^{-1}; Wallace and Beavan, 2010) and slow slip rates (6.9 mmday^{-1}; Ikari et al., 2020) converted to reference (shaded) shear strain rates for a ~33 m-wide fault core.

gradients that drive the dissolution of frictionally stronger minerals, substantial reductions in fault strength can occur via frictional-viscous flow, even without pore fluid overpressures (Niemeijer, 2018; Phillips and White, 2017; Wallis et al., 2015).

Employing the microphysical model for frictional-viscous flow developed by Bos and Spiers (2002), we estimate the shear stresses required to generate deformation in the ~33-m wide Hungaroa fault core (Fig. 12). The flow law for frictional-viscous flow is written as:

$$\tau = \tau_{gb} + \left\{ \left(\tau_{ps}\right)^{-p} + \left(\tau_{dil}\right)^{-p} \right\}^{-1/p} \quad (2)$$

and in our application, τ_{gb} is the shear stress required for frictional sliding over a smectite (montmorillonite) foliation, τ_{ps} is the shear stress required for isovolumetric pressure solution of calcite grains/microlithons in the shear direction, τ_{dil} is the shear stress required for dilatation of calcite grains/microlithons during granular flow, and p is an exponent that controls the switch from pressure solution to dilatation, here taken to be 20, indicative of an instantaneous transition between the two processes (Niemeijer and Spiers, 2005). Because pressure solution abruptly transitions to dilatation, calcite either accommodates shear strain via pressure solution or via dilatational granular flow in the model. In the Hungaroa fault core, only the brittle cross-cutting faults contain random-fabric gouges interpreted to have formed during dilatational granular flow (Figs. 3b, 4h–j).

The magnitude of the stress gradient driving DMT was calculated using a geometry constrained by the mean microlithon aspect ratio (3.2) and a diffusion length scale (d), defined as the distance between the calcite source and sink, set equal to the length of a calcareous microlithon long axis (Fig. 5). We account for microstructural observations that microlithon long-axis lengths varied depending on structural setting, lithology, and unsealed fracture density, by exploring a range of possible diffusion length scales. Using the diffusion length scales, a fluid film thickness of 10^{-8} m, the solubility of calcite at 80 °C (1.186^{-5} m^{3}m^{-3}; Plummer and Busenberg, 1982), and an experimentally determined diffusion coefficient (2.568^{-10} m^{3}s^{-1}; Nakashima, 1995), calcite diffusive fluxes were calculated and set equal to the microlithon-scale shear strain rate. The maximum diffusion length scale limits the net shear strain rate that can be accommodated via DMT. To obtain shear strain rates across the width of the HFZ, results of the microphysical model were scaled up by assuming all the foliation planes in the tabular shear zone were undergoing simple shear and were deforming simultaneously via diffusion-controlled pressure solution creep (Fig. 12 and caption) (Bos et al., 2000b; Bos and Spiers, 2002; Rutter and Mainprice, 1979).

The modelled fault zone displays three distinct fault strength regimes, with the transition between each regime controlled primarily by the kinetic parameters of DMT, such as the diffusion length scale (Fig. 12). Increasing temperature only has a minor effect on pressure solution rates, because an increase in the diffusion coefficient counteracts the decrease in calcite solubility (e.g., Gratier et al., 2013). At low strain rates ($\dot{\gamma} \leq 10^{-9}$ s^{-1} for d = 0.1 mm), the DMT of calcite requires little shear stress and fault strength is controlled by the rate-dependent friction coefficient of the S_1 foliation and the effective normal stress. The S_1 foliation friction coefficient is calculated using the friction coefficient of pure montmorillonite ($\mu = 0.11$) at a reference strain rate of 10^{-4} s^{-1} and becomes weaker by a friction rate parameter (a–b) of +0.0004 with each decade (×10) decrease in strain rate (Morrow et al., 2017). At 3 km depth on the HFZ, the effective normal stress was calculated by setting the least principal stress (σ_3) equal to the overburden stress, letting the shear zone with $\mu = 0.11$ lie 10° to the maximum principal stress (σ_1), and evaluating both hydrostatic ($\lambda = 0.4$) and sub-lithostatic ($\lambda = 0.9$) pore fluid pressures (cf. Fig. 12 and caption). For a diffusion length scale of 0.1 mm, an increase in shear zone dip of 30° is needed to double the strain rate at which the transition from non-dilatant to dilatant sliding occurs, a result that reflects the small dependence of the foliation's shear resistance on effective normal stress.

In the low strain-rate, non-dilatant regime, the Bos and Spiers (2002) model is distinct from den Hartog and Spiers (2014), who assumed that shear stress is controlled by pressure solution of the soluble phase, rather than the frictional properties of the foliation. This assumption leads to a

decrease in fault strength with increasing proportions of the soluble phase, which does not agree with results from rock analogue experiments (Bos et al., 2000a) or microstructural observations of the Hungaroa fault core, where calcite-rich lithologies form phacoids (Fig. 3). The presence of clays promotes diffusion-controlled pressure solution creep by inhibiting healing along grain boundary contacts, increasing fluid film thickness, maintaining pore connectivity, and allowing grain boundary sliding to occur at lower contact stresses (e.g., Gratier et al., 2013; Niemeijer and Spiers, 2005; Renard et al., 2001; Viti et al., 2014). Because of these factors, an interconnected phyllosilicate foliation can increase the diffusive flux and decrease the shear stress needed for DMT.

At intermediate strain rates (10^{-9} s^{-1}< $\dot{\gamma}$ <3×10^{-6} s^{-1} for d = 0.1 mm), the shear stresses required for DMT of calcite start to contribute to fault strength. Fault strength increases with increasing strain rate by an amount larger than that predicted by the rate-and-state friction equations (Eq. 1, 2) (Fig. 12) (Dieterich, 1979; Scholz, 1998). At fast strain rates ($\dot{\gamma}$ >3×10^{-6} s^{-1} for d = 0.1 mm), pressure solution is too slow to accommodate the imposed strain rate, and dilatation with calcite fragmentation, translation, and rotation (i.e., cataclastic granular flow) occurs. Within this regime, the S_1 foliation is destroyed, and the friction coefficient is determined by the proportion of calcite and phyllosilicates in the fault rock (e.g., Boulton et al., 2019). To capture the maximum possible strength of the fault at fast strain rates, our model employs the sliding friction coefficient of pure calcite (μ = 0.65) (Verberne et al., 2014), and the effective normal stresses at 3 km depth for a shear zone dipping 10° to σ_1. A significant result of the modelling is that, for diffusion length scales up to d = 0.3 mm, the friction coefficient of the clay foliation controls fault strength at plate convergence strain rates. In contrast, at the strain rates of slow slip events, a diffusion length scale of d = 0.3 mm already results in significant strengthening (or strain rate hardening) due to the kinetics of diffusion-controlled pressure solution creep (Fig. 12). Overall, matrix strengthening at a given depth can occur via: (1) a decrease in the kinetics of pressure solution (e.g., through an increase in the diffusion length scale); (2) a decrease in the thickness of the zone undergoing frictional-viscous flow (a type of geometric strengthening); (3) an increase in the coefficient of friction; and/or (4) a decrease in pore fluid pressure.

At the low deformation temperatures in the Hungaroa fault zone (71–92 °C), calcite is reported to deform primarily by twinning, cataclasis and/or grain-size sensitive processes such as pressure solution creep (e.g., Ebert et al., 2007; Kennedy and White, 2001) (cf. Figs. 4, 6, 8). However, low-temperature plasticity in calcite grains is well-documented, and debate remains as to whether high strain rate laboratory experiments on calcite can adequately capture deformation that occurs at lower strain rates over geological timescales (e.g., Bauer et al., 2018; Kennedy and White, 2001; Liu et al., 2002; Molli et al., 2011). Fig. 12 shows the predicted shear stress that would result from cross-slip accommodated dislocation creep in calcite, the principal low-temperature crystal plastic deformation mechanism in calcite (De Bresser, 2002). The frictional-viscous flow law of Bos and Spiers (2002) indicates that the maximum (brittle) fault strength at 3 km depth is below the shear stress required to deform calcite via cross-slip accommodated dislocation creep. This theoretical result, combined with our microstructural observations, indicates that diffusion-controlled pressure solution creep was the dominant deformation mechanism active in the Hungaroa fault core (Fig. 12). Diffusion-controlled pressure solution creep in fine-grain calcareous mudstones is capable of accommodating slip at the low shear stresses that drive movement on low-angle thrust faults, including subduction megathrusts.

8. Conclusions

Active as an early Miocene landward-verging thrust, the Hungaroa fault zone accommodated deformation via distributed slip across a ~33 m-wide zone containing a S-C′ tectonite fabric developed in calcareous, smectitic mudstones of the Middle to Late Eocene Wanstead Formation. Lithologically similar hemipelagic and pelagic sediments were deposited across the East Coast Basin and subducting Pacific Plate during the Paleogene (Field and Uruski, 1997; "Sequence Y" of Davy et al., 2008; Burgreen-Chan et al., 2016). Marine seismic surveys, validated by scientific drilling in ODP Leg 181 and IODP Expedition 375, show that the shallow Hikurangi Subduction Zone décollement also localizes in this sequence, which is punctuated in places by seamounts (e.g., Barnes et al., 2020; Ghisetti et al., 2016). Temperatures of HFZ deformation (T = 71–92 °C), constrained by clumped isotope thermometry of syntectonic calcite veins, exist throughout the upper 8–12 km of the subduction zone megathrust fault (Fagereng and Ellis, 2009).

HFZ deformation took place in a ~33 m-wide high-strain fault core, and individual strands of subduction zone plate boundary faults commonly have similar thicknesses (Rowe et al., 2013). Discrete brittle faults form the fault core boundaries and locally cross-cut the S_1 foliation and C′-shears, but deformation was mainly accommodated by diffusion-controlled pressure solution creep in the calcareous mudstone matrix. The Hungaroa fault core resembles the continuous deformation dominant mélange described in Fagereng et al. (2010), and we modelled the rheology as frictional-viscous flow following Bos and Spiers (2002) and Niemeijer and Spiers (2005). At low strain rates, the Hungaroa fault zone would have deformed at very low shear stresses (τ < 10 MPa), with extensional calcite veins oriented at low and high angles to the S_1 foliation providing evidence of periodic (lithostatic) pore fluid overpressures.

Within the calcite veins, elongate blocky and stretched fiber calcite crystal habits reflect incremental sealing by calcite-bearing diagenetic fluids. Diffusion-controlled pressure solution creep on the S_1 foliation resulted in measurable stress heterogeneities within the fault core. At shallow depths (<4 km), creep within the fault core accommodated permanent (irrecoverable) strain, thus limiting the elastic strain energy available for earthquake rupture propagation (e.g., Wang et al., 2021). Even at a constant stress, fault zones deforming via frictional-viscous flow can exhibit variable strain rates — from plate rates to slow slip rates and full locking — if processes such as the grain-scale or fracture-scale change the diffusion length. Thus, we suggest that the shallow (up-dip) limit of the seismogenic zone is not a simple function of temperature in fault zones governed by a frictional-viscous flow rheology (e.g., Bos and Spiers, 2002; Fagereng and Beall, 2021). Rather, faults with macro- to-microscale structures like the Hungaroa fault zone have seismic potentials controlled by the spatiotemporally variable properties of their constitutive fluids and fault rocks.

Author contributions

Carolyn Boulton: Conceptualization, Methodology, Formal analysis, Investigation, Writing - Original Draft, Review & Editing, Visualization, Project administration, and Funding acquisition. **Marcel Mizera**: Methodology, Formal analysis, Investigation, Writing - Original Draft, Review & Editing, Visualization. **André R. Niemeijer**: Methodology, Formal analysis, Investigation, Writing - Review & Editing, Resources, Visualization, Funding acquisition. **Timothy A. Little**: Investigation, Formal analysis, Writing - Review & Editing. **Inigo A. Müller**: Investigation, Formal analysis, Writing - Review & Editing. **Martin Ziegler**: Investigation, Resources, Writing - Review & Editing. **Maartje F. Hamers**: Investigation, Formal analysis, Writing - Review & Editing.

Declaration of Competing Interest

The authors declare that they have no known competing financial interests or personal relationships that could have appeared to influence the work reported in this paper.

Acknowledgements

Funding for this research was provided by a Royal Society of New

Zealand Rutherford postdoctoral fellowship (C.B.), NZ Ministry for Business, Innovation, and Employment Endeavour Fund CO5X1605 subcontract (C.B.), the New Horizons for Women Trust Margaret L. Bailey Science Award (C.B.), European Plate Observing System (EPOS) Trans-National Access Grants (C.B.), and Dutch Research Council (NWO) DEEPNL grant 2018.040 (A.R.N.). The authors benefitted from helpful discussions with Susan Ellis, Hans De Bresser, David Wallis, Chris Hollis, and Ben Hines. Arnold van Dijk provided analytical support, and thin sections were prepared by Stuart Bush, Rob Spiers, and Leonard Bik. Mark Raven expertly performed the QXRPD analyses. Marco Herwegh, Ake Fagereng, and an anonymous reviewer provided constructive comments that significantly improved the manuscript.

Appendix A. Supplementary data

Supplementary data to this article can be found online at https://doi.org/10.1016/j.lithos.2022.106831.

References

Anderson, N.T., Kelson, J.R., Kele, S., Daëron, M., Bonifacie, M., Horita, J., et al., 2021. A unified clumped isotope thermometer calibration (0.5–1100°C) using carbonate-based standardization. Geophysical Research Letters 48 (7) e2020GL092069.

Arslan, A., Passchier, C.W., Koehn, D., 2008. Foliation boudinage. Journal of Structural Geology 30 (3), 291–309.

Ashtari, M., Mousavi, S.E., Cheshomi, A., Khamechian, M., 2019. Evaluation of the single compressive strength test in estimating uniaxial compressive and Brazilian tensile strengths and elastic modulus of marlstone. Engineering Geology 248, 256–266.

Ballance, P.F., 1976. Evolution of the Upper Cenozoic Magmatic Arc and plate boundary in northern New Zealand. Earth and Planetary Science Letters 28 (3), 356–370.

Barnes, P.M., de Lépinay, B.M., Collot, J.-Y., Delteil, J., Audru, J.-C., 1998. Strain partitioning in the transition area between oblique subduction and continental collision, Hikurangi margin, New Zealand. Tectonics 17 (4), 534–557.

Barnes, P.M., Nicol, A., Harrison, A., 2002. Late Cenozoic evolution and earthquake potential of an active listric thrust complex, Hikurangi subduction margin, New Zealand. Geological Society of America Bulletin 114, 1379–1405.

Barnes, P.M., Wallace, L.M., Saffer, D.M., Bell, R.E., et al., 2020. Slow slip source characterized by lithological and geometric heterogeneity. Science Advances 6 (13). https://doi.org/10.1126/sciadv.aay3314.

Bauer, H., Rogowitz, A., Grasemann, B., Decker, K., 2018. Intracrystalline deformation of calcite in the upper brittle crust. Geology 46 (4), 375–378.

Beall, A., Fagereng, Å., Ellis, S., 2019. Strength of strained two-phase mixtures: application to rapid creep and stress amplification in subduction zone mélanges. Geophysical Research Letters 46. https://doi.org/10.1029/2018GL081252.

Beanland, S., Haines, A.J., 1998. A kinematic model of active deformation in the North Island, New Zealand, determined from geological strain rates. New Zealand Journal of Geology and Geophysics 41, 311–323.

Beavan, J., Tregoning, P., Bevis, B., Kato, T., Meertens, C., 2002. The motion and rigidity of the Pacific Plate and implications for plate boundary deformation. Journal of Geophysical Research 107 (B10), 2261.

Begg, J.G., Johnston, M.R., 2000. Geology of the Wellington Area, 10. Institute of Geological and Nuclear Sciences Geological Map scale 1:250,000, 1 sheet + 64 pp, Lower Hutt.

Behr, W.M., Platt, J.P., 2014. Brittle faults are weak, yet the ductile middle crust is strong: implications for lithospheric mechanics. Geophysical Research Letters 41 (22), 8067–8075.

Bernasconi, S.M., Daëron, M., Bergmann, K.D., Bonifacie, M., Meckler, A.N., et al., 2021. Intercarb: a community effort to improve interlaboratory standardization of the carbonate clumped isotope thermometer using carbonate standards. Geochemistry, Geophysics, Geosystems 22. https://doi.org/10.1029/2020GC009588.

Bons, P.D., 2001. Development of crystal morphology during unitaxial growth in a progressively widening vein: 1. The numerical model. Journal of Structural Geology 23, 865–872.

Bons, P.D., Elburg, M.A., Gomez-Rivas, E., 2012. A review of the formation of tectonic veins and their microstructures. Journal of Structural Geology 43, 33–62.

Bos, B., Spiers, C.J., 2002. Frictional-viscous flow of phyllosilicate-bearing fault rock: microphysical model and implications for crustal strength profiles. Journal of Geophysical Research 107 (B2), 2028.

Bos, B., Peach, C.J., Spiers, C.J., 2000a. Frictional-viscous flow of simulated fault gouge caused by the combined effects of phyllosilicates and pressure solution. Tectonophysics 327, 173–194.

Bos, B., Peach, C.J., Spiers, C.J., 2000b. Slip behavior of simulated gouge-bearing faults under conditions favoring pressure solution. Journal of Geophysical Research - Solid Earth 105, 16699–16717.

Boulton, C., Niemeijer, A.R., Hollis, C.J., Townend, J., Raven, M.D., Kulhanek, D.K., Shepherd, C.L., 2019. Temperature-dependent frictional properties of heterogeneous Hikurangi Subduction Zone input sediments, ODP Site 1124. Tectonophysics 757, 123–139.

Burgreen-Chan, B., Graham, S.A., 2018. Petroleum system modeling of the East Coast Basin, Hawke Bay, New Zealand. American Association of Petroleum Geologists Bulletin 102 (4), 587–612.

Burgreen-Chan, B., Meisling, K.E., Graham, S., 2016. Basin and petroleum system modelling of the East Coast Basin, New Zealand: a test of overpressure scenarios in a convergent margin. Basin Research 28, 536–567.

Burkhard, M., 1993. Calcite twins, their geometry, appearance and significance as stress-strain markers and indicators of tectonic regime: a review. Journal of Structural Geology 15 (3–5), 351–368.

Chanier, F., Ferriere, J., 1991. From a passive to an active margin: tectonic and sedimentary processes linked to the birth of an accretionary prism (Hikurangi Margin, New Zealand). Bulletin. Société Géologique de France 162, 649–660.

Collettini, C., Tesei, T., Scuderi, M.M., Carpenter, B.M., Viti, C., 2019. Beyond Byerlee friction, weak faults and implications for slip behavior. Earth and Planetary Science Letters 519, 245–263.

Colton-Bradley, V.A., 1987. Role of pressure in smectite dehydration: Effects on geopressure and smectite-to-illite transformation. The American Association of Petroleum Geologists Bulletin 71 (11), 1414–1427.

Davy, B., Hoernle, K., Werner, R., 2008. Hikurangi Plateau: crustal structure, rifted formation, and Gondwana subduction history. Geochemistry, Geophysics, Geosystems 9 (7), Q07004.

De Bresser, J.H.P., 2002. On the mechanism of dislocation creep of calcite at high temperature: Inferences from experimentally measured pressure sensitivity and strain rate sensitivity of flow stress. Journal of Geophysical Research - Solid Earth 107 (B12), 2337.

Delteil, J., Morgans, H.E.G., Raine, J.I., Field, B.D., Cutten, H.N.C., 1996. Early Miocene thin-skinned tectonics and wrench faulting in the Pongaroa district, Hikurangi margin, North Island, New Zealand. New Zealand Journal of Geology and Geophysics 39, 271–282.

den Hartog, S.A.M., Spiers, C.J., 2014. A microphysical model for fault gouge friction applied to subduction megathrusts. Journal of Geophysical Research - Solid Earth 119, 1510–1529.

den Hartog, S.A.M., Niemeijer, A.R., Spiers, C.J., 2012. New constraints on megathrust slip stability under subduction zone P-T conditions. Earth and Planetary Science Letters 353–354, 240–252.

DeReuil, A.A., Birgenheier, L.P., McLennan, J., 2019. Effects of anisotropy and saturation on geomechanical behavior of mudstone. Journal of Geophysical Research - Solid Earth 124, 8101–8126.

Dieterich, J., 1979. Modeling of rock friction 1. Experimental results and constitutive equations. Journal of Geophysical Research 84 (B5), 2162–2168.

Ebert, A., Herwegh, M., Pfiffner, A., 2007. Cooling induced strain localization in carbonate mylonites within a large-scale shear zone (Glarus thrust, Switzerland). Journal of Structural Geology 29, 1164–1184.

Evans, M.A., Dunne, W.M., 1991. Strain factorization and partitioning in the North Mountain thrust sheet, Central Appalachians, USA. Journal of Structural Geology 13 (1), 21–35.

Evans, M.A., Groshong Jr., R.H., 1994. A computer program for the calcite strain-gauge technique. Journal of Structural Geology 16 (2), 277–281.

Fagereng, Å., Beall, A., 2021. Is complex fault zone behaviour a reflection of rheological heterogeneity? Philosophical Transactions of the Royal Society A 379, 20190421.

Fagereng, Å., Ellis, S., 2009. On factors controlling the depth of interseismic coupling on the Hikurangi subduction interface, New Zealand. Earth and Planetary Science Letters 278 (1/2), 120–130.

Fagereng, Å., Remitti, F., Sibson, R.H., 2010. Shear veins observed within anisotropic fabric at high angles to the maximum compressive stress. Nature Geoscience 3, 482–485.

Fagereng, Å., Diener, J.F.A., Ellis, S., Remitti, F., 2018. Fluid-related deformation processes at the up- and downdip limits of the subduction thrust seismogenic zone: What do the rocks tell us? In: Byrne, T., Underwood, M.B., Fisher, D., McNeill, L., Saffer, D., Ujiie, K., Yamaguchi, A. (Eds.), Geology and Tectonics of Subduction Zones: A Tribute to Gaku Kimura, Geological Society of America Special Paper, vol. 534, pp. 187–215.

Faulkner, D.R., Sanchez-Roa, C., Boulton, C., den Hartog, S.A.M., 2018. Pore fluid pressure development in compacting fault gouge in theory, experiments, and nature. Journal of Geophysical Research - Solid Earth 123. https://doi.org/10.1002/2017JB015130.

Fagereng, Å., 2013. On stress and strain in a continuous-discontinuous shear zone undergoing simple shear and volume loss. Journal of Structural Geology 50, 44–53.

Ferrill, D.A., 1998. Critical re-evaluation of differential stress estimates from calcite twins in coarse-grained limestone. Tectonophysics 285 (1–2), 77–86.

Ferrill, D.A., Morris, A.P., Evans, M.A., Burkhard, M., Groshong Jr., R.H., Onasch, C.M., 2004. Calcite twin morphology: a low-temperature deformation geothermometer. Journal of Structural Geology 26 (8), 1521–1529.

Field, B.D., Uruski, C.I., 1997. Cretaceous-Cenozoic geology and petroleum systems of the East Coast Region, New Zealand. In: Institute of Geological and Nuclear Sciences Monograph 19, 301 Pp. GNS Science, Lower Hutt.

Finch, M.A., Bons, P.D., Steinbach, F., Griera, A., Llorens, M.-G., Gomez-Rivas, E., Ran, H., de Riese, T., 2020. The ephemeral development of C' shear bands: A numerical modelling approach. Journal of Stuctural Geology 139. https://doi.org/10.1016/j.jsg.2020/104091.

Folk, R.L., 1959. Practical classification of limestones. American Association of Petroleum Geologists Bulletin 43 (1), 1–38.

French, M.E., Condit, C.B., 2019. Slip partitioning along an idealized subduction plate boundary at deep slow slip conditions. Earth and Planetary Science Letters 528, 115828.

Furlong, K.P., Kamp, P.J.J., 2009. The lithospheric geodynamics of plate boundary transpression in New Zealand: initiating and emplacing subduction along the Hikurangi margin, and the tectonic evolution of the Alpine Fault system. Tectonophysics 474 (3–4), 449–462.
Gharechelou, S., Amini, A., Bohloli, B., Swennen, R., 2020. Relationship between the sedimentary microfacies and geomechanical behaviour of the Asmari Formation carbonates, southwestern Iran. Marine and Petroleum Geology 116, 104306.
Ghisetti, F.C., Barnes, P.M., Ellis, S., Plaza-Faverola, A.A., Barker, D.H.N., 2016. The last 2 Myr of accretionary wedge construction in the Central Hikurangi margin (North Island, New Zealand): insights from structural modeling. Geochemistry, Geophysics, Geosystems 17 (7), 2661–2686.
Ghosh, P., Adkins, J., Affek, H., Balta, B., Guo, W., Schauble, E.A., Schrag, D., Eiler, J.M., 2006. ^{13}C–^{18}O bonds in carbonate minerals: a new kind of paleothermometer. Geochimica et Cosmochimica Acta 70, 1439–1456.
Goodwin, L.B., Tikoff, B., 2002. Competency contrast, kinematics, and the development of foliations and lineations in the crust. Journal of Structural Geology 24, 1065–1085.
Gratier, J.-P., Thouvenot, F., Jenatton, L., Tourette, A., Doan, M.-L., Renard, F., 2013. Geological control of the partitioning between seismic and aseismic sliding behaviours in active faults: evidence from the Western Alps, France. Tectonophysics 600, 226–242.
Hansen, E., 1971. Strain Facies, 207 pp.. Springer-Verlag, New York.
Hasegawa, M., Yoshida, K., Asano, Y., Okada, T., Iinuma, T., Ito, Y., 2012. Change in stress field after the great Tohoku-oki earthquake. Earth and Planetary Science Letters 355–356, 231–243.
Hemmingway, J.D., Henkes, G.A., 2021. A disordered kinetic model for clumped isotope bond reordering in carbonates. Earth and Planetary Science Letters 566. https://doi.org/10.1016/j.epsl.2021.116962.
Henkes, G.A., Passey, B.H., Grossman, E.L., Shenton, B.J., Pérez-Huerta, A., Yancey, T.E., 2014. Temperature limits for preservation of primary calcite clumped isotope paleotemperatures. Geochimica et Cosmochimica Acta 139, 362–382.
Henrys, S., Wech, A., Sutherland, R., Stern, T., Savage, M., Sato, H., Mochizuki, K., Iwasaki, T., Okaya, D., Seward, A., Tozer, B., Townend, J., Kurashimo, E., Iidaka, T., Ishiyama, T., 2013. SAHKE geophysical transect reveals crustal and subduction zone structure at the southern Hikurangi margin, New Zealand. Geochemistry, Geophysics, Geosystems 14, 2063–2083.
Hines, B.R., Kulhanek, D.K., Hollis, C.J., Atkins, C.B., Morgans, H.E.G., 2013. Paleocene-Eocene stratigraphy and paleoenvironment at Tora, Southeast Wairarapa, New Zealand. New Zealand Journal of Geology and Geophysics 56 (4), 243–262.
Hubbert, M.K., Rubey, W.W., 1959. Role of fluid pressure in mechanics of overthrust faulting. Bulletin Geological Society of America 70, 115–166.
Huntington, K.W., Lechler, A.R., 2015. Carbonate clumped isotope thermometry in continental tectonics. Tectonophysics 647–648, 1–20.
Ikari, M.J., Wallace, L.M., Rabinowitz, H.S., Savage, H.M., Hamling, I.J., Kopf, A.J., 2020. Observations of laboratory and natural slow slip events: Hikurangi subduction zone, New Zealand. Geochemistry, Geophysics, Geosystems 21 (2), e2019GC008717.
Jiao, R., Seward, D., Little, T.A., Kohn, B.P., 2014. Thermal history and exhumation of basement rocks from Mesozoic to Cenozoic subduction cycles, central North Island, New Zealand. Tectonics 33, 1920–1935.
Jiao, R., Seward, D., Little, T.A., Kohn, B.P., 2015. Unroofing of fore-arc ranges along the Hikurangi Margin, New Zealand: constraints from low-temperature thermochronology. Tectonophysics 656, 39–51.
Kennedy, L.A., White, J.C., 2001. Low-temperature recrystallization of calcite: mechanisms and consequences. Geology 29, 1027–1030.
Kim, S.T., O'Neil, J.R., 1997. Equilibrium and non-equilibrium oxygen isotope effects in synthetic carbonates. Geochimica et Cosmochimica Acta 61, 3461–3475.
Kurzawski, R.M., Niemeijer, A.R., Stipp, M., Charpentier, D., Behrmann, J.H., Spiers, C. J., 2018. Frictional properties of subduction input sediments at an erosive convergent continental margin and related controls on décollement slip modes: the Costa Rica Seismogenesis Project. Journal of Geophysics Solid Earth 123, 8386–8408.
Lacombe, O., Parlangeau, C., Beaudoin, N.E., Amrouch, K., 2021. Calcite twin formation, measurement and use as stress-strain indicators: a review of progress over the last decade. Geosciences 11, 445. https://doi.org/10.3390/geosciences11110445.
Laird, M.G., Bassett, K.N., Schiøler, Morgans, Bradshaw, J.D., Weaver, S.D., 2003. Paleoenvironmental and tectonic changes across the Cretaceous/Tertiary boundary at Tora, southeast Wairarapa, New Zealand: a link between Marlborough and Hawke's Bay. New Zealand Journal of Geology and Geophysics 46, 275–293.
Lamb, S., 2011. Cenozoic tectonic evolution of the New Zealand plate-boundary zone: a paleomagnetic perspective. Tectonophysics 509, 135–164.
Leah, H., Fagereng, Å., Meneghini, F., Morgan, J.K., Savage, H.M., Wang, M., Bell, R., Ikari, M.J., 2020. Mixed brittle and viscous strain localization in pelagic sediments seaward of the Hikurangi Margin, New Zealand. Tectonics 39. https://doi.org/10.1029/2019TC005965.
Liu, J., Walter, J.M., Weber, K., 2002. Fluid-enhanced low-temperature plasticity of calcite marble: microstructures and mechanisms. Geology 30 (9), 787–790.
Liu, Z., Pagani, M., Zinniker, D., DeConto, R., Huber, M., Brinkhuis, H., Shah, S.R., Leckie, R.M., Pearson, A., 2009. Global cooling during the Eocene-Oligocene climate transition. Science 323, 1187–1190.
Luetkemeyer, P.B., Kirschner, D.L., Huntington, K.W., Chester, J.S., Chester, F.M., Evans, J.P., 2016. Constraints on paleofluid sources using the clumped-isotope thermometry of carbonate veins from the SAFOD (San Andreas Fault Observatory at Depth) borehole. Tectonophysics 690, 174–189.
Maison, T., Potel, S., Malié, P., Mählmann, R.F., Chanier, F., Mahieux, G., Bailleul, J., 2018. Low-grade evolution of clay minerals and organic matter in fault zones of the Hikurangi prism (New Zealand). Clay Minerals 53, 579–602.
Marone, C., 1998. Laboratory-derived friction laws and their application to seismic faulting. Annual Reviews of Earth and Planetary Sciences 26, 643–696.
Meckler, A.N., Ziegler, M., Millán, M.I., Breitenbach, S.F.M., Bernasconi, S.M., 2014. Long-term performance of the Kiel carbonate device with a new correction scheme for clumped isotope measurements. Rapid Communications in Mass Spectrometry 28 (15), 1705–1715. https://doi.org/10.1002/rcm.6949.
Mizera, M., Little, T.A., Boulton, C., Prior, D.J., Watson, E., Biemiller, J., White, J., Shigematsu, N., 2020. Slow-to-fast deformation in mafic fault rocks on an active low-angle normal fault, Woodlark Rift, SE Papua New Guinea. Geochemistry, Geophysics, Geosystems 21 e2020GC009171.
Meneghini, F., Moore, J.C., 2007. Deformation and hydrofracture in a subduction thrust at seismogenic depths: the Rodeo Cove thrust zone, Marin Headlands, California. Geological Society of America Bulletin 119 (1/2), 174–183.
Mizera, M., Little, T.A., Boulton, C., Katzir, Y., Thiagarajan, N., Prior, D.J., Biemiller, J., Smith, E.G.C., 2021. Using syntectonic calcite veins to reconstruct the strength evolution of an active low-angle normal fault, Woodlark Rift, SE Papua New Guinea. Journal of Geophysical Research - Solid Earth 126 (8), e2021JB021916.
Molli, G., White, J.C., Kennedy, L., Taini, V., 2011. Low-temperature deformation of limestone, Isola Palmaria, northern Appenine, Italy – the role of primary textures, precursory veins and intracrystalline deformation in localization. Journal of Structural Geology 33, 255–270.
Morrow, C.A., Moore, D.E., Lockner, D.A., 2017. Frictional strength of wet and dry montmorillonite. Journal of Geophysical Research - Solid Earth 122, 3392–3409.
Mortimer, N., 2004. New Zealand's geological foundations. Gondwana Research 7 (1), 261–272.
Mortimer, N., van den Bogaard, P., Hoernle, K., Timm, C., Gans, P.B., Werner, R., Riefstahl, F., 2019. Late Cretaceous oceanic plate reorganization and the breakup of Zealandia and Gondwana. Gondwana Research 65, 31–42.
Nakashima, S., 1995. Diffusivity of ions in pore water as a quantitative basis for rock deformation rate estimates. Tectonophysics 245, 185–203.
Nicol, A., Wallace, L., 2007. Temporal stability of deformation rates: comparison of geological and geodetic observations, Hikurangi subduction margin, New Zealand. Earth and Planetary Science Letters 258, 397–413.
Nicol, A., Mazengarb, C., Chanier, F., Rait, G., Uruski, C., Wallace, L., 2007. Tectonic evolution of the active Hikurangi subduction margin, New Zealand, since the Oligocene. Tectonics 26, TC4002.
Niemeijer, A.R., 2018. Velocity-dependent slip weakening by the combined operation of pressure solution and foliation development. Scientific Reports 8, 4724. https://doi.org/10.1038/s41598-018-22889-3.
Niemeijer, A.R., Spiers, C.J., 2005. Influence of phyllosilicates on fault strength in the brittle–ductile transition: Insights from rock analogue experiments. In: Bruhn, D., Burlini, L. (Eds.), Deformation Mechanisms Rheology and Tectonics, 245. Geological Society of London, pp. 303–327.
Niemeijer, A.R., Spiers, C.J., Peach, C.J., 2008. Frictional behaviour of simulated quartz fault gouges under hydrothermal conditions: results from ultra-high strain rotary shear experiments. Tectonophysics 460, 288–303.
O'Neil, J.R., Clayton, R.N., Mayeda, T.K., 1969. Oxygen isotope fractionation in divalent metal carbonates. The Journal of Chemical Physics 51, 5547–5558.
Passchier, C.W., Trouw, R.A.J., 2005. Microtectonics, second ed. Springer Verlag, Berlin.
Pettinga, J., 1982. Upper Cenozoic structural history, coastal southern Hawkes Bay, New Zealand. New Zealand Journal of Geology and Geophysics 25, 149–191.
Phillips, N.J., White, J.C., 2017. Grain size-dependent strength of phyllosilicate-rich gouges in the shallow crust: Insights from the SAFOD site. Journal of Geophysical Research - Solid Earth 122, 5789–5812.
Picard, M.D., 1971. Classification of fine-grained sedimentary rocks. Journal of Sedimentary Petrology 41, 179–195.
Plank, T., 2014. The chemical composition of subducting sediments. Treatise on Geochemistry 4, 607–629.
Plummer, L.N., Busenberg, E., 1982. The solubilities of calcite, aragonite and vaterite in CO_2-H_2O solutions between 0 and 90°C and an evaluation of the aqueous model for the system $CaCO_3$-CO_2-H_2O. Geochimica et Cosmochimica Acta 46, 1011–1040.
Rait, G., Chanier, F., Waters, D., 1991. Landward and seaward-directed thrusting accompanying the onset of subduction beneath New Zealand. Geology 19, 230–233.
Raven, M.D., Self, P.G., Gomez-Camacho, R., 2018. XRD Report – Quantitative XRD Analysis of Samples VUW HFZ Shale for Victoria University of Wellington. CSIRO Land and Water, Urrbrae, South Australia, New Zealand.
Renani, H.R., Martin, C.D., 2018. Cohesion degradation and friction mobilization in brittle failure of rocks. International Journal of Rock Mechanics and Mining Sciences 106, 1–13.
Renard, F., Gratier, J.-P., Jamtveit, B., 2000. Kinetics of crack-sealing, intergranular pressure solution, and compaction around active faults. Journal of Structural Geology 22, 1395–1407.
Renard, F., Dysthe, D., Feder, J., Bjorlykke, K., Jamtveit, B., 2001. Enhanced pressure solution creep rates induced by clay particles: experimental evidence in salt aggregates. Geophysical Research Letters 28, 1295–1298.
Rowe, C., Moore, J.C., Remitti, F., IODP Expedition 343/343T Scientists, 2013. The thickness of subduction plate boundary faults from the seafloor into the seismogenic zone. Geology 41 (9), 991–994.
Ruina, A., 1983. Slip instability and state variable laws. Journal of Geophysical Research 88 (B12), 10359–10370.
Rutter, E.H., 1976. The kinetics of rock deformation by pressure solution. Philosophical Transactions of the Royal Society of London 283, 203–219.
Rutter, E.H., Mainprice, D.H., 1979. On the possibility of slow fault slip controlled by a diffusive mass transfer process. Gerlands Beiträge zur Geophysik, Leipzig 88, 154–162.

Rybacki, E., Evans, B., Janssen, C., Wirth, R., Dresen, G., 2013. Influence of stress, temperature, and strain on calcite twins constrained by deformation experiments. Tectonophysics 601, 20–36.
Saffer, D.M., Tobin, H.J., 2011. Hydrogeology and mechanics of subduction zone forearcs: fluid flow and pore pressure. Annual Review of Earth and Planetary Sciences 39 (1), 157–186.
Scholz, C.H., 1998. Earthquakes and friction laws. Nature 391, 37–42.
Secor, D.T., 1965. Role of fluid pressure in jointing. American Journal of Science 263, 633–646.
Sibson, R.H., 1977. Fault rocks and fault mechanisms. Journal of the Geological Society 133 (3), 191–213.
Sibson, R.H., 1985. A note on fault reactivation. Journal of Structural Geology 7 (6), 751–754.
Sibson, R.H., 2009. Rupturing in overpressured crust during compressional inversion–the case from NE Honshu, Japan. Tectonophysics 473 (3–4), 404–416.
Sibson, R.H., 2017. Tensile overpressure compartments on low-angle thrust faults. Earth, Planets and Space 69, 113.
Smeraglia, L., Bernasconi, S.M., Berra, F., Billi, A., Boschi, C., Caracausi, A., Carminati, E., Castorina, F., Doglioni, C., Italiano, F., Luca Rizzo, A., Uysal, I., Zhao, J., 2018. Crustal-scale fluid circulation and co-seismic shallow comb-veining along the longest normal fault of the central Apennines, Italy. Earth and Planetary Science Letters 498, 152–168.
Stolper, D.A., Eiler, J.M., 2015. The kinetics of solid-state isotope-exchange reactions for clumped isotopes: a study of inorganic calcites and apatites from natural and experimental samples. American Journal of Science 315, 363–411.
Sutherland, R., Stagpoole, V., Uruski, C., Kennedy, C., Bassett, D., Henrys, S., Scherwath, M., Kopp, H., Field, B., Toulmin, S., Barker, D., Bannister, S., Davey, F., Stern, T., Flueh, E.R., 2009. Reactivation of tectonics, crustal underplating, and uplift after 60 Myr of passive subsidence, Raukumara Basin, Hikurangi-Kermadec fore arc, New Zealand: implications for global growth and recycling of continents. Tectonics 28, TC5017.
Tesei, T., Collettini, C., Viti, C., Barchi, M.R., 2013. Fault architecture and deformation mechanisms in exhumed analogues of seismogenic carbonate-bearing thrusts. Journal of Structural Geology 55, 167–181.
Tippett, J.M., Kamp, P.J.J., 1993. Fission track analysis of the Late Cenozoic vertical kinematics of continental Pacific Crust, South Island, New Zealand. Journal of Geophysical Research 98 (B9), 16119–16148.
Turner, F.J., 1953. Nature and dynamic interpretation of deformation lamellae in calcite of three marbles. American Journal of Science 251 (4), 276–298.
Ujiie, K., Saishu, H., Fagereng, Å., Nishiyama, N., Otsubo, M., Masuyama, H., Kagi, H., 2018. An explanation of episodic tremor and slow slip constrained by crack-seal veins and viscous shear in subduction mélange. Geophysical Research Letters 45, 5371–5379.
van den Ende, M.P.A., Chen, J., Niemeijer, A.R., Ampuero, J.-P., 2020. Rheological transitions facilitate fault-spanning ruptures on seismically active and creeping faults. Journal of Geophysical Research - Solid Earth 125. https://doi.org/10.1029/2019JB019328.
Verberne, B., Spiers, C.J., Niemeijer, A.R., De Bresser, J.H.P., de Winter, D.A.M., Plümper, O., 2014. Frictional properties and microstructures of calcite-rich fault gouges sheared at sub-seismic sliding velocities. Pure and Applied Geophysics 171, 2617–2640.
Viti, C., Collettini, C., Tesei, T., 2014. Pressure solution seams in carbonatic fault rocks: mineralogy, micro/nanostructures and deformation mechanism. Contributions to Mineralogy and Petrology 167, 970.
Wallace, L.M., Beavan, J., 2010. Diverse slow slip behavior at the Hikurangi subduction margin, New Zealand. Journal of Geophysical Research 115, B12402.
Wallis, D., Lloyd, G.E., Phillips, R.J., Parsons, A.J., Walshaw, R.D., 2015. Low effective fault strength due to frictional-viscous flow in phyllonites, Karakoram Fault Zone, NW India. Journal of Structural Geology 77, 45–61.
Wang, K., Zhu, Y., Nissen, E., Shen, Z.-K., 2021. On the relevance of geodetic deformation rates to earthquake potential. Geophysical Research Letters 48. https://doi.org/10.1029/2021GL093231.
Webber, S., Ellis, S., Fagereng, Å., 2018. "Virtual shear box" experiments of stress and slip cycling within a subduction interface mélange. Earth and Planetary Science Letters 488, 27–35.
Zhang, X., Spiers, C.J., Peach, C.J., 2010. Compaction creep of wet granular calcite by pressure solution at 28°C to 150°C. Journal of Geophysical Research 115. https://doi.org/10.1029/2008JB005853.